

Landslide kinematics and their potential controls from hourly to decadal timescales: Insights from integrating ground-based InSAR measurements with structural maps and long-term monitoring data

William H. Schulz^{a,*}, Jeffrey A. Coe^a, Pier P. Ricci^b, Gregory M. Smoczyk^a, Brett L. Shurtleff^{a,1}, Joanna Panosky^{a,1}

^a U.S. Geological Survey, Box 25046, MS-966, Denver, CO 80225, USA

^b Ingegneria Dei Sistemi, Via Enrica Calabresi, 24 - Loc. Montacchiello, 56121 Pisa, Italy

ARTICLE INFO

Article history:

Received 5 April 2016

Received in revised form 1 February 2017

Accepted 18 February 2017

Available online 21 February 2017

Keywords:

Landslide

Earthflow

InSAR

Kinematics

Slumgullion

Stress transfer

ABSTRACT

Knowledge of kinematics is rudimentary for understanding landslide controls and is increasingly valuable with greater spatiotemporal coverage. However, characterizing landslide-wide kinematics is rare, especially at broadly ranging timescales. We used highly detailed kinematic data obtained using photogrammetry and field mapping during the 1980s and 1990s and our 4.3-day ground-based InSAR survey during 2010 to study kinematics of the large, persistently moving Slumgullion landslide. The landslide was segregated into 11 kinematic elements using the 1980s–1990s data and the InSAR survey revealed most of these elements within a few hours. Averages of InSAR-derived displacement point measures within each element agreed well with higher quality in situ observations; averaging was deemed necessary because adverse look angles for the radar coupled with tree cover on the landslide introduced error in the InSAR results. We found that the landslide moved during 2010 at about half its 1985–1990 speed, but slowing was most pronounced at the landslide head. Gradually decreased precipitation and increased temperature between the periods likely resulted in lower groundwater levels and consequent slowing of the landslide. We used GPS survey results and limit-equilibrium modeling to analyze changing stability of the landslide head from observed thinning and found that its stability increased between the two periods, which would result in its slowing, and the consequent slowing of the entire landslide. Additionally, InSAR results suggested movement of kinematic element boundaries in the head region and our field mapping verified that they moved and changed character, likely because of the long-term increasing head stability. On an hourly basis, InSAR results were near error bounds but suggested landslide acceleration in response to seemingly negligible rainfall. Pore-pressure diffusion modeling suggested that rainfall infiltration affected frictional strength only to shallow depths along the landslide's marginal faults, highlighting their importance in controlling landslide stability. Hourly results also suggested that motion propagated along the 3.9-km length of the active landslide, even following sub-millimeter displacements, while strengthening of landslide shear boundaries during faster movement was likely critical in regulating the landslide's motion. Hence, detailed kinematic characterizations obtained from traditional and emerging approaches helped to reveal that mechanisms controlling landslide movement and evolution over decades also are critical to sub-millimeter movement on a nearly continuous basis.

Published by Elsevier B.V. This is an open access article under the CC BY license (<http://creativecommons.org/licenses/by/4.0/>).

1. Introduction

Landslides sculpt hillslopes, denude mountain ranges, weather and transport soil and rock, and present significant hazards to human safety and the built environment. Studies indicate that landslides are the dominant process controlling hillslope geomorphology and hydrology in

many regions (e.g., Schmidt and Montgomery, 1995; Burbank et al., 1996; Roering et al., 2009). Annually, landslides cause >3.5 billion USD in property damage (U.S. Geological Survey, 2005) and loss of thousands of lives (Petley, 2012) worldwide. Hence, great efforts are made to understand how landslides move and mechanisms controlling their movement in order to forecast the evolution of Earth's surface and hazards landslides present. Perhaps the most rudimentary knowledge required for understanding landsliding mechanisms and effects is that of kinematics. Knowledge of kinematics helps to reveal temporally and spatially variable stresses acting within landslides, their boundary

* Corresponding author.

E-mail address: wschulz@usgs.gov (W.H. Schulz).

¹ Formerly with the affiliation they are linked to.

geometries, mechanical properties of materials composing landslides, external forcing conditions, and characteristics of future landslide movement.

Landslides often comprise different kinematic elements, and conditions affecting their movement, such as material properties and pore-water pressures, vary in time and space. Hence, landslide kinematic characterization benefits greatly from increased spatiotemporal resolution. Traditionally, spatially dense kinematic data are acquired by mapping landslide features in the field and from aerial photographs to provide temporally discrete characterizations (e.g., Baum et al., 1993, 1998; Smith, 1993; Fleming et al., 1999; Baldi et al., 2008; Coe et al., 2016). Multiple such characterizations are used to reveal landslide motion generally at annual–decadal timescales (e.g., Parise, 2003; Mackey et al., 2009; Mackey and Roering, 2011; Giordan et al., 2013; Guerriero et al., 2014). Recently, the traditional tools have been supplemented by analyses of remotely sensed data. Repeated acquisitions of highly detailed topographic data from lidar may be used to estimate movement of landslides, including at timescales as short as days (e.g., Oppikofer et al., 2009; Prokop and Panholzer, 2009; Aryal et al., 2012; Jaboyedoff et al., 2012). Interferometric synthetic aperture radar (InSAR) methods using data acquired from aerial and satellite platforms may reveal movement of the ground surface at daily to monthly timescales, including movement related to landslides (e.g., Rott et al., 1999; Bürgmann et al., 2000; Schmidt and Bürgmann, 2003; Hilley et al., 2004; Roering et al., 2009; Calabro et al., 2010; Cascini et al., 2010; Handwerger et al., 2013, 2015; Milillo et al., 2014; Schlögel et al., 2015). Ground-based InSAR (GBInSAR) and interferometric real aperture radar are capable of repeatedly surveying landslide areas within minutes with up to millimeter-level accuracy and have been used successfully for measuring landslide kinematics (e.g., Pieraccini et al., 2003; Tarchi et al., 2003; Antonello et al., 2004; Gischig et al., 2009; Barla et al., 2010; Casagli et al., 2010; Lowry et al., 2013). GBInSAR also shows promise for revealing short-term (e.g., hourly or less) differential landslide motion (e.g., Tarchi et al., 2003; Lowry et al., 2013). Spatially dense kinematic data provided by the traditional and more recently developed approaches have proven useful for evaluating landslide evolution and mechanisms controlling their movement; however, much remains to be learned about the evolution of landslide movement and controls thereon,

particularly in the short-term for which temporal relations between landslide kinematic elements remain unclear.

We used exceptionally detailed kinematic and structural documentation from the period 1985–1993 (Smith, 1993; Fleming et al., 1999) and GBInSAR displacement data acquired for four days during 2010 to evaluate movement of the large, persistent, well-studied Slumgullion landslide located in Colorado, USA (Fig. 1). We evaluated mechanisms responsible for observed kinematics using data obtained from monitoring of meteorological and groundwater conditions. Our study provides unique views of landslide kinematics and their potential controls at a weekly timescale, and of kinematic evolution over several decades. The study also provides an opportunity to evaluate the ability of GBInSAR for characterizing landslide kinematics compared to traditional approaches. Additionally, our GBInSAR results may reveal for the first time the spatially extensive interplay of landslide kinematic elements at a timescale commensurate with landslide motion.

2. The Slumgullion landslide

The Slumgullion landslide has long been studied. Although first mentioned in a scientific paper during the late 1800s and thought to be deposits from alluvial, glacial, and/or snow avalanche processes (Endlich, 1876), the first accurate description of it as a landslide was from the 1883 confession of the notorious “Colorado cannibal” Alferd Packer who reported (e.g., Gant, 1952) that he left the scene of his crime located adjacent to the landslide by following a big slide of yellowish clay. Later studies revealed it to be a 3.9-km-long, slowly moving, persistent, translational landslide nested within a larger, dormant landslide deposit (e.g., Varnes and Savage, 1996). Slumgullion is best classified as a debris slide (Cruden and Varnes, 1996) because nearly all of its motion appears to occur by sliding along faults bounding the landslide (e.g., Fleming et al., 1999) and it contains >20% sand and coarser material (Schulz et al., 2007, 2009a). Total displacements of hundreds of meters (e.g., Fleming et al., 1999; Coe et al., 2009) result in morphology suggestive of flow and it has been referred to as an earthflow previously (e.g., Keefer and Johnson, 1983; Gombert et al., 1995; Varnes and Savage, 1996). The active part of the landslide and the underlying landslide deposit comprise deeply weathered Tertiary basalt, rhyolite, and

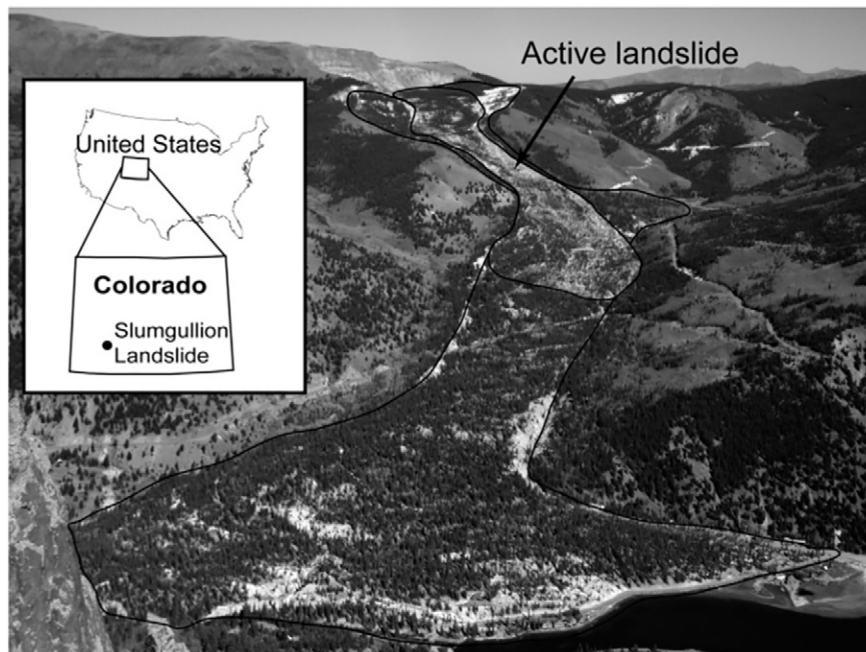


Fig. 1. Location map and photograph showing the Slumgullion landslide. The actively moving part is indicated; lines extending beyond the active part approximately delineate the inactive landslide deposit. The active landslide is 3.9 km long.

andesite (Lipman, 1976). Weathering products include angular volcanic rock fragments and silt and clay consisting of smectite and kaolinite with high plasticity (Chleborad et al., 1996; Schulz et al., 2007, 2009a). The active landslide has an average ground surface of 8°, estimated volume of $20 \times 10^6 \text{ m}^3$, and estimated average thickness of 13 m (Parise and Guzzi, 1992). The landslide spans elevations between 3000 and 3700 m and occupies the montane and subalpine ecological zones (Löve, 1970), with sporadic coverage by Engelmann spruce and quaking aspen trees.

Slumgullion moves almost entirely by sliding along faults (e.g., Crandell and Varnes, 1961; Gomberg et al., 1995; Fleming et al., 1999). Although often considered only in the context of tectonics, faults by definition also apply to landslides as they are approximately planar surfaces caused by failure and across which relative displacement occurs. Many landslide studies have recognized this (e.g., Keefer and Johnson, 1983; Fleming and Johnson, 1989; Fleming et al., 1999; Parise, 2003; Coe et al., 2009; Guerriero et al., 2014) and landslide faults have been specifically referenced and studied as analogs to tectonic faults (e.g., Peng and Gomberg, 2010), including at Slumgullion (e.g., Gomberg et al., 1995, 2011; Walter et al., 2013). Strike-slip faults form the landslide's lateral margins, generally occur within flank ridges, and periodically relocate (e.g., Cross, 1909; Fleming et al., 1999; Parise, 2003; Schulz et al., 2009a, b). The landslide toe advances over the former ground surface, bulldozing and engulfing vegetation as it moves along (e.g., Guzzi and Parise, 1992; Fleming et al., 1999; Coe et al., 2003, 2009). Spatially variable speeds generally within $0.25\text{--}7 \text{ m year}^{-1}$ have been observed at the ground surface by many researchers (e.g., Crandell and Varnes, 1961; Smith, 1993; Fleming et al., 1999; Coe et al., 2003, 2009; Parise et al., 2003; Schulz et al., 2007, 2009a, 2012; Coe, 2012), with fastest speeds near the longitudinal center of the landslide and slowest speeds near the landslide head and toe. The spatial speed variability is manifested by distinct kinematic elements that are generally bounded by faults, folds, and fractures (Guzzi and Parise, 1992; Fleming et al., 1999; Coe et al., 2003). Presumably, these elements largely result from variations in landslide basal topography that appears to have remained constant at least for much of the 20th century (Fleming et al., 1999; Parise et al., 2003; Coe et al., 2009).

Current activity of the Slumgullion landslide appears to have been triggered 300–400 years ago by gravitational failure of rock and soil onto the formerly dormant landslide head (Crandell and Varnes, 1961; Varnes and Savage, 1996; Fleming et al., 1999). Fleming et al. (1999) concluded that the landslide currently is slowing because geomorphic evidence indicates that the upper half of the landslide is thinner than it was previously, while the landslide toe is thicker and wider; hence, driving stress is decreasing while resisting stress is increasing. This thinning of the upper part of the landslide was supported by analyses of aerial photographs from 1939/40–2000 whereas the toe was observed to advance 92 m during this period (Coe et al., 2009). Slowing of at least the upper part of the landslide is supported by measurements by Coe et al. (2003), who observed that the landslide head moved more slowly during 1999–2001 than during the mid-1980s–early 1990s. Multi-year monitoring efforts (Savage and Fleming, 1996; Coe et al., 2003; Parise et al., 2003; Schulz et al., 2007, 2009a) identified slowest movement of the landslide during winter, when most precipitation falls as snow, and fastest movement during peak snowmelt and significant rainfall events. Coe et al. (2003) observed that the lower part of the landslide accelerated in the spring prior to the upper part during some years, likely due to snowmelt occurring earlier on the lower part of the landslide. Maximum speeds following snowmelt and rainfall typically were within ~170% of annual average speeds (Coe et al., 2003; Schulz et al., 2007, 2009a). Coe et al. (2003) and Schulz et al. (2007, 2009a) provided evidence to support the general conclusions that landslide speed directly correlates with pore-water pressure. They observed that landslide speed increased when pore-water pressures within the landslide body were relatively high and decreased when pressures were relatively low. Schulz et al. (2007, 2009a) observed that pore-water pressures

increased within hours to a few days following significant rainfall and snowmelt events, and that the landslide speed responded contemporaneously with pressure changes. However, this relation held true only for pore pressures measured within the landslide body. Schulz et al. (2007, 2009a) observed at a location along one of the landslide's marginal strike-slip faults that pore-water pressures decreased during significant acceleration periods and increased during deceleration. They concluded that accelerated shear-induced dilation along the landslide's bounding faults could cause reduced pore-water pressure and consequent strengthening of the faults, helping to regulate the landslide's speed. The landslide's movement has appeared to be sensitive to seemingly negligible forcing as well. Coe et al. (2003) suggested that the landslide's speed may vary in response to changing atmospheric pressure, and Schulz et al. (2009b) observed direct correlations between low atmospheric tides and landslide acceleration, which they concluded likely resulted from tidally induced variations in effective normal stress along landslide shear zones and consequent variations in shear strength. Their conclusions were supported by passive seismic monitoring (Gomberg et al., 2011) that showed increased occurrence of slidequakes during low atmospheric tides.

3. Methods

The less-than-ideal setting for GBInSAR study at Slumgullion may be typical for many landslides; tree cover is relatively dense, atmospheric and soil-moisture conditions may vary spatially along the landslide's great length and elevation range, and limited locations for setting the radar resulted in adverse view angles. Therefore, we used additional techniques to measure landslide movement during the survey and we also monitored groundwater and meteorological conditions. We used results from detailed studies performed during the 1980s and 1990s (Smith, 1993; Fleming et al., 1999) to develop a kinematic framework for the landslide that we subsequently used to evaluate kinematics during the GBInSAR survey and long-term kinematic change.

3.1. Delineation of kinematic elements

As observed previously (e.g., Smith, 1993; Gomberg et al., 1995; Fleming et al., 1999; Coe et al., 2003), the Slumgullion landslide comprises multiple kinematic elements, each of which moves similar to a rigid block by sliding along faults. We used highly detailed mapping of Fleming et al. (1999) and point measures of annual average speed from Smith (1993; these speeds are provided also on Fleming et al.'s (1999) maps) to delineate 11 primary kinematic elements forming the landslide. Although Fleming et al. (1999) performed their mapping during 1992 and 1993 while Smith's (1993) measurements spanned 1985–1990, we assumed that features mapped by Fleming et al. (1999) largely resulted from spatially variable landslide basal topography that remains temporally consistent; hence, structures they mapped during 1992 and 1993 should have closely correlated spatially with identical structures during 1985–1990. Coe et al. (2009) found that many topographic and hydrologic features such as depressions and ponds on the landslide remained spatially stationary for 60–300 years while the landslide moved through these locations, supporting temporal consistency of the landslide's basal topography.

We georeferenced the maps from Fleming et al. (1999) by aligning their topographic contours outside of the landslide to those geocoded by Messerich and Coe (2003); inspection suggested georeferencing error of less than a meter. Fleming et al. (1999) mapped the landslide in the field at 1:1000 scale with assistance from aerial photographs taken on August 25, 1990 and a topographic map derived from the photographs. They believed that features they mapped were generally accurately located within a few meters. Smith (1993) used the same aerial photographs (1:6000 scale) and others taken on August 12, 1985 (1:12,000 scale) to map the locations and displacements of 310 natural features on the landslide. Duplicate measures of control points indicated

a standard deviation of apparent displacements of 0.6 m. We used mapped major faults and fracture zones from Fleming et al. (1999) and significant variations of Smith's (1993) 1985–1990 average speeds to delineate the kinematic elements. However, the landslide toe advances over the ground surface so we adjusted the distal boundary of the toe to account for movement since Fleming et al.'s (1999) work using U.S. Department of Agriculture National Agriculture Imagery Program (NAIP) imagery dated Sept. 24, 2013 and available through ESRI's ArcGIS server (30 cm resolution). Smith's (1993) speeds were then averaged within each of the elements. This provided a clear basis for comparison with displacements observed during the GbInSAR survey of the landslide.

3.2. GbInSAR survey

Our GbInSAR survey was performed using the IBIS-L developed by IDS (Ingegneria dei Sistemi, Pisa, Italy). The IBIS-L consists of a portable, stepped-frequency, continuous-wave radar working in the Ku frequency band that moves across a 2-m-long rail while taking measurements, hence, the synthetic aperture. As with all radar systems, displacement measurements are limited to the line of sight of the instrument and we set the IBIS-L so that its line of sight was oriented downhill and sub-parallel to the length of the landslide. IBIS Guardian software automatically processed acquired data using the persistent scatterers approach (e.g., Ferretti et al., 2001), which includes applying corrections for atmospheric effects. The software and approaches utilized therein are proprietary. As configured for our survey, the IBIS-L had a range resolution of 1 m and cross-range resolution of 4.4 mrad. Processed displacement data had 1-m pixel resolution. According to IDS, processed IBIS-L data are capable of providing 0.1 mm displacement accuracy during field studies at distances up to 4 km. Testing of the similar IBIS-S system indicated accuracy better than 0.02 mm at a distance of 7 m in the laboratory (Gentile and Bernardini, 2009) and accuracy of ± 0.004 mm for displacements of 0.05 mm at a distance of 16 m outdoors (Xing et al., 2014). Dehls et al. (2010) estimated ± 1 mm accuracy for the IBIS-L during a 2-week-long survey at distances up to 3.2 km.

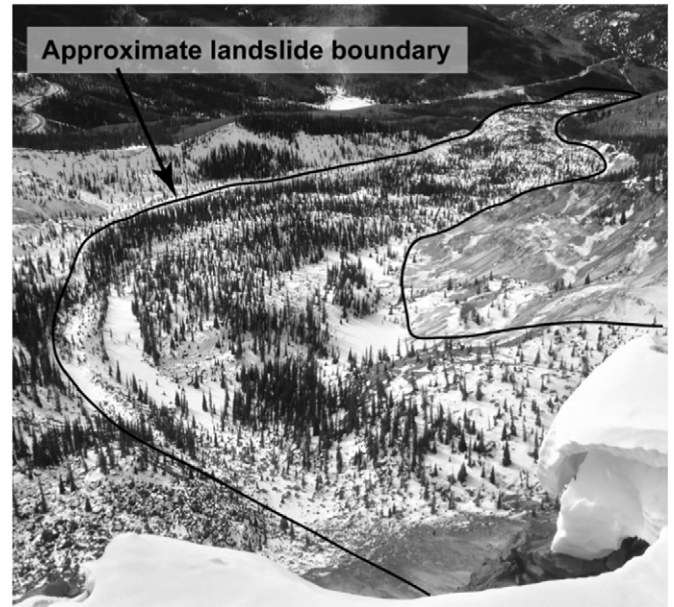


Fig. 3. View similar to that of the IBIS-L during the survey. The IBIS-L was located ~200 m to the left of the photographer. A winter photograph (December 10, 2015) is provided to better illustrate tree cover on the landslide and surrounding area. The active landslide is 3.9 km long.

We installed the IBIS-L on the crest of the landslide headscarp (Fig. 2) with a view subparallel to most of the landslide movement direction (e.g., Smith, 1993) (Fig. 3). We bolted the instrument to ~200 kg of concrete blocks placed on gravel that we compacted by hand on in situ weathered basalt. The instrument operated continuously from 6/26/2010 17:21 to 7/1/2010 0:57 and processed data were obtained for hourly intervals. We used differential GPS surveying of the ends of the IBIS-L's linear rail to provide a basis for determining georeferenced measurements; error in the GPS measurements necessitated a 0.5° rotation

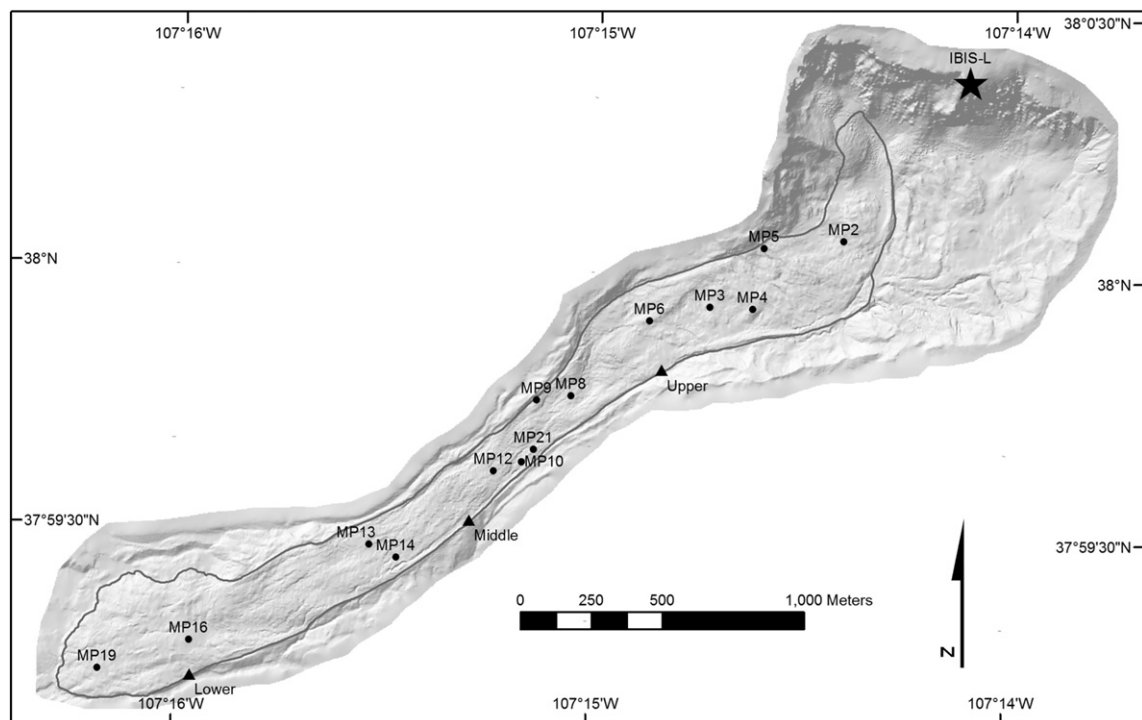


Fig. 2. Map of landslide and monitoring locations. Base is shaded relief derived from Messerich and Coe (2003); the active landslide boundary is shown as a gray line and was modified from Fleming et al. (1999); and locations of the IBIS-L, GPS monuments (MP#), and monitoring stations (upper, middle, and lower) used during the study also are provided.

of the data (clockwise about the origin) to better fit the landslide boundaries mapped from Fleming et al. (1999). The downward look angle from the IBIS-L to the landslide surface ranged between 10 and 24°, so we projected displacement measures to the horizontal plane for comparison with previous long-term studies and to the landslide surface for evaluation of short-term results. We averaged displacements within each kinematic element for clarity and to permit comparison with previous studies. Buffers of 10 m were first applied to both sides of element boundary lines to exclude InSAR data from these areas and reduce the potential for misrepresentation of displacements due to errors in mapping and georeferencing.

A great benefit of InSAR for measuring landslide displacement is that no physical contact with moving ground is required, thus removing the potential for interference and sensor destruction from movement as is inherent with use of most in situ sensors. However, radar measurements may be obtained from any objects in the field of view, including unstable objects such as trees and other vegetation. For our survey, radar returns from vegetation were certainly common (Fig. 3). We attempted to reduce the number of these returns in the final displacement dataset by using data only with relatively high return signal intensity and with overall non-negative line-of-sight displacement. Negative displacements indicate movement toward the IBIS-L, or in the upslope direction. However, it is likely that many data points still represented measures from vegetation. Additionally, apparent InSAR-derived displacements may be affected by changes in atmospheric conditions (e.g., temperature, humidity, solar radiation, and pressure) and soil moisture, so we delineated “control regions” outside of the landslide adjacent to each kinematic element to permit direct comparison of apparent displacements in spatially contiguous areas on and off the landslide. The landslide may often experience spatially variable atmospheric and soil moisture conditions because of its great size and elevation range.

3.2.1. In situ monitoring

For comparison with GBInSAR results, we measured positions of 13 monuments on the landslide (Fig. 2) near the beginning and end of the InSAR survey period using differential GPS surveying techniques. We continuously measured the position of one location (MP21) on the landslide throughout the survey period, also using differential GPS. Continuous measurements were obtained for 5-s epochs and subsequently smoothed using a 1-h moving average. However, data were not obtained between 6/29/2010 4:03 and 6/29/2010 14:05 (58.70–68.73 elapsed hours) because of power loss. Displacement results from all measurements were projected to the planimetric line of sight of the IBIS-L for comparison. Campaign-style GPS surveys used for the 13 monuments are considered accurate to approximately ± 15 mm.

We measured hourly displacement at three monitoring stations on the landslide using temporarily and permanently installed cable extension transducers (extensometers) (Fig. 2). Each sensor crossed the strike-slip fault bounding the landslide. The extensometers have stated accuracy of ± 1 mm and resolution of ~ 0.4 mm; however, the extensometers and their anchors were mounted to posts ~ 3 m above the ground surface and utilized several meters of extension cable to reduce the potential for damage from wildlife, so accuracy was reduced. Temporary installations utilized 4.1-cm-diameter, 16-gauge steel posts driven into the ground and ~ 5 –20 m of Invar extension cable, whereas permanent installations utilized 6.0-cm-diameter, 12-gauge steel posts set in concrete and ~ 5 m of Invar extension cable. The upper site utilized a temporary extensometer for the duration of the study while temporary extensometers were used at the middle and lower sites at the onset of the survey period. Permanent extensometers were utilized beginning at 6/30/2010 15:10 (93.82 elapsed hours) for the middle site and 6/27/2010 19:35 (26.23 elapsed hours) for the lower site. Data gaps of ~ 7 h exist for these two extensometers and approximate offsets derived from displacement trends were added to the post-gap extensometer records to account for the missing data (2.0 mm and 1.4 mm for the middle and lower extensometers, respectively).

Pore-water pressures were measured at each of the monitoring stations using non-vented, vibrating-wire piezometers with stated accuracy of ± 0.345 kPa and resolution of 0.086 kPa. Installation of piezometers was ongoing during the InSAR survey period. Each was installed in the landslide by direct burial within a borehole 1–4 m in-board from the strike-slip fault bounding the south side of the landslide. The upper site piezometer was installed 5.71 m below the ground surface and was operational throughout the study. The middle site piezometer was installed 9.14 m below the ground surface and was operational throughout the study except for 6/29/2010 7:00 to 6/30/2010 15:10 (61.65 to 93.82 elapsed hours). The lower site piezometer was installed 4.57 m below the ground surface and was operational beginning 6/30/2010 14:20 (92.98 elapsed hours).

We measured rainfall at the middle monitoring site using a tipping-bucket rain gauge with 0.254 mm resolution and accuracy of ± 0.00254 mm until 6/29/2010 7:00 (61.65 elapsed hours). Rainfall data after this period were obtained from a MesoWest weather station (DW0739) located in Lake City, approximately 6.7 km northwest from the middle site (MesoWest, 2016). Atmospheric pressure data also were obtained from the MesoWest station for the duration of the study.

3.2.2. Long-term meteorological monitoring

Meteorological conditions have not been monitored at the landslide for most of our 30-year study period. Precipitation and air temperature data were collected beginning during 1980 and 1983, respectively, by the U.S. Department of Agriculture Slumgullion SNOTEL meteorological station located 4 km east of the landslide center approximately at the elevation of the landslide head (SNOTEL Slumgullion, 2016). The Slumgullion SNOTEL station did not collect air temperature data during July 1993–August 1995 so we also obtained data from the Beartown SNOTEL station (SNOTEL Beartown, 2016) located 41 km southwest of the landslide for this period. We offset the Beartown data by -0.35 °C to account for the average temperature difference between the stations during the nine months prior to and following the data gap at Slumgullion.

4. Results

4.1. 1985–1990 kinematics

The primary kinematic elements the landslide comprises (Fig. 4) had average speeds during Aug. 1985–Aug. 1990 of 2.0–14.4 mm d⁻¹ (Table 1). The number of individual speed measurements available for each element ranged between 4 and 64, and speeds within each element displayed standard deviations of 2.4 mm d⁻¹ or less (Table 1). Elements 1–5 form the flattest part of the landslide and speeds increased nearly linearly in the downslope direction from element 1 to element 4 (Fig. 5). Although the upper part of element 1 is quite steep (see Messerich and Coe, 2003, for details), the middle part is nearly flat (3°) and this element moved slowest. The ground surface steepens downhill from elements 1 and 2 and is pervasively dissected by normal faults (see Fleming et al., 1999, for details) that cross much of the landslide's width. Most displacement along the faults is in the downhill direction but some upslope-facing normal faults occur also and partly bound extensional grabens. Element 3 is nearly unfaulted while its boundary with element 4 consists of en echelon fractures and normal faults indicative of left-lateral motion as element 4 moves away from element 3. A series of downslope-directed normal faults form most of the downslope boundary of element 4, with right-lateral movement occurring along the western part of its boundary with element 5. Speed increased abruptly from elements 4 to 5 and increased nearly linearly in the downslope direction for elements 4 through 7. The landslide steepens markedly in the upper half of element 6 (16°) compared to element 5 (3°) and it also narrows, both of which likely resulted in element 6 having been markedly faster than element 5. Normal faults that transect the width of the landslide occur throughout the upper part of element 6

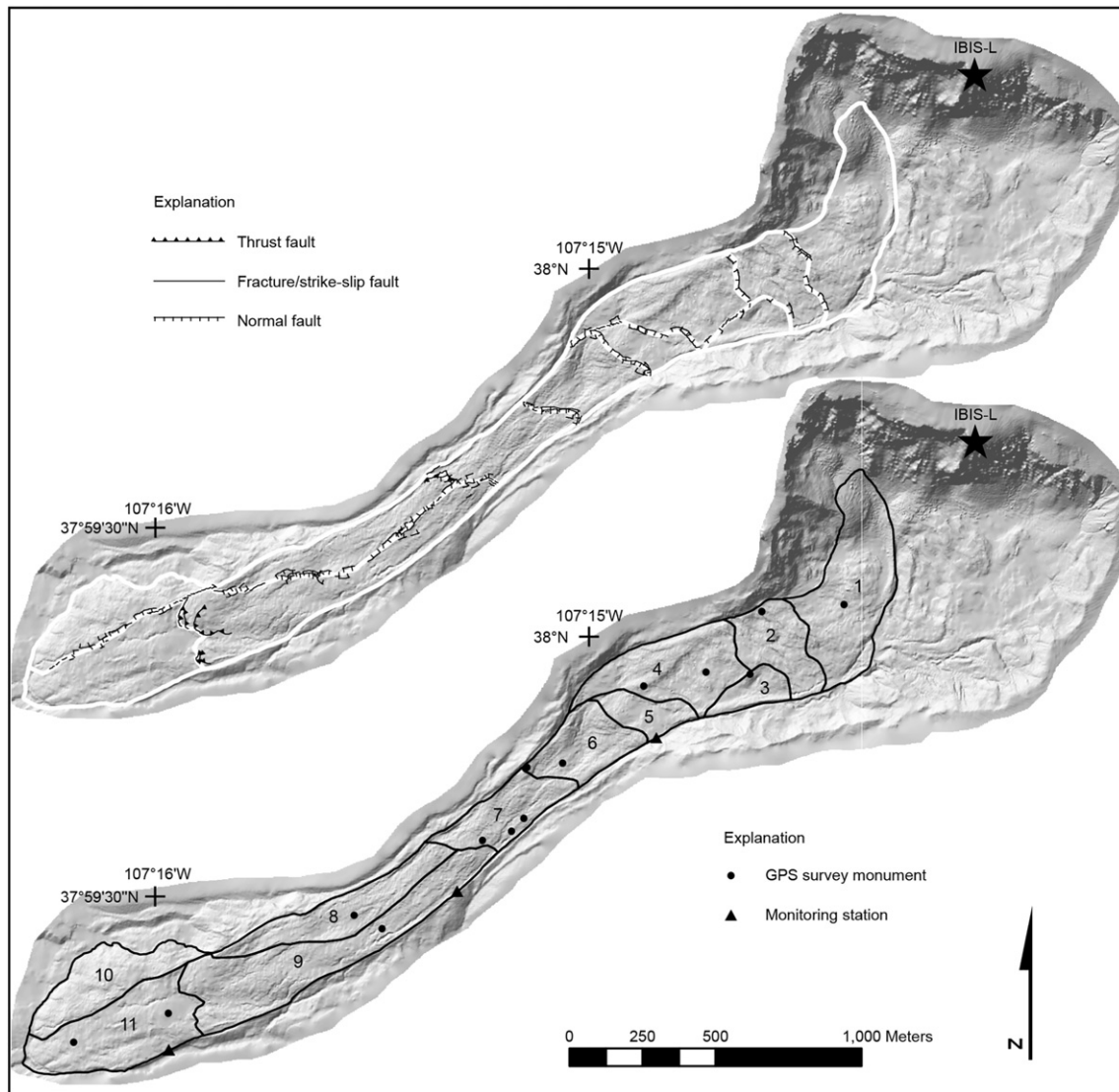


Fig. 4. Maps showing kinematic elements. Upper map shows simplification of structures mapped by Fleming et al. (1999) used to delineate element boundaries, which are shown in white; speeds measured by Smith (1993) also used for delineating kinematic elements are not shown for clarity. Lower map shows element boundaries in black and provides element names (1–11). Locations of in situ monitoring also are shown on the lower map but not labeled for clarity; monitoring sites are defined on Fig. 2.

while thrust faults similarly occupy the central part of the element above a flatter region. Element 7 was the fastest part of the landslide, being separated from element 6 by a region of normal faults and pervasive fracturing, and it is the steepest (9°) element of the landslide (element 6 averages 7°). The landslide slowed downslope from element 7 as it widens and subtly flattens; elements 8 and 9 slope 8° , on average. Normal faults, many of which are directed upslope, and pervasive fracturing separate element 7 from 8 and 9. Elements 8 and 9 moved nearly the same speed but are separated by a series of normal faults directed toward either landslide margin. The downslope end of element 9 displays multiple thrust faults and corresponds with the inferred location of the landslide toe where it emerged from the ground surface following landslide initiation (e.g., Parise and Guzzi, 1992; Fleming et al., 1999). Downslope from this location, the landslide moves along the former ground surface forming elements 10 and 11, which moved much slower than elements 8 and 9. Excluding the steep leading edge of the landslide toe at the downslope ends of elements 10 and 11, these elements are on average 2° flatter than elements 8 and 9. En echelon fractures, normal faults, and right-lateral strike-slip faults separate elements 10 and 11. The average element speeds from 1985 to 1990 (Table 1) suggest that

20–130 m of landslide movement occurred between 1985 and 2010 when our GBInSAR survey was performed.

4.2. 2010 kinematics from GBInSAR

The IBIS-L obtained data continuously for 103.6 h and generally returned $\sim 41,000$ point measurements during each scan. Removal of points with relatively low return intensity and overall negative uphill displacement resulted in an average of 34,219 retained point measurements per scan. Of these, 28,697 were from the landslide and 5522 were from areas outside of the slide, on average (Table 1). Total displacements for landslide points were as great as 154 mm (Fig. 6) but most displacements (98.3%) were 55 mm or less. Displacements within given kinematic elements were generally consistent but differed between elements (Fig. 6). The maximum displacement measured within control regions outside of the landslide (designated by apostrophes on Fig. 6 and in the text) was 46 mm. Average displacements of points within control regions increased nearly linearly downslope; in terms of speed, control region 1' displayed the lowest average downslope speed of 0.4 mm d^{-1} whereas region 89' displayed the greatest average

Table 1
Average speeds.

| Kinematic element or control region | 1985–1990 Average speed (mm d ⁻¹) | 1985–1990 Std. dev. (mm d ⁻¹) | 2010 Average speed (mm d ⁻¹) | Average GBInSAR Measurement count | 2010 Std. dev. (mm d ⁻¹) | 2010 speed/ 1985–1990 speed |
|-------------------------------------|---|---|--|---|--|--------------------------------|
| Landslide | 6.8 | 3.8 | 3.2 | 28,697 | 3.7 | 47% |
| 1 | 2.0 | 1.1 | 0.4 | 3093 | 2.5 | 18% |
| 2 | 3.3 | 0.7 | 0.9 | 1731 | 3.5 | 28% |
| 3 | 3.9 | 0.4 | 1.0 | 658 | 3.6 | 25% |
| 4 | 4.4 | 1.4 | 1.0 | 6164 | 2.7 | 23% |
| 5 | 6.7 | 0.8 | 2.9 | 1997 | 4.2 | 43% |
| 6 | 10.6 | 2.4 | 4.6 | 2521 | 6.9 | 44% |
| 7 | 14.4 | 2.0 | 7.8 | 2258 | 9.2 | 54% |
| 8 | 9.8 | 1.1 | 4.5 | 2816 | 8.6 | 46% |
| 9 | 10.0 | 2.4 | 5.3 | 4505 | 8.4 | 53% |
| 10 | 4.3 | 0.5 | 2.5 | 55 | 17.8 | 60% |
| 11 | 5.4 | 1.0 | 3.1 | 2900 | 6.5 | 58% |
| Outside | | | 1.2 | 5522 | 1.5 | |
| 1' | | | 0.4 | 3350 | 1.1 | |
| 2' | | | 0.5 | 57 | 4.5 | |
| 3' | | | 0.8 | 441 | 3.8 | |
| 4' | | | 1.1 | 1129 | 2.0 | |
| 5' | | | 1.0 | 457 | 3.4 | |
| 6' | | | 1.8 | 293 | 5.2 | |
| 7' | | | 1.9 | 266 | 7.9 | |
| 89' | | | 2.1 | 352 | 8.4 | |
| 1011' | | | 1.3 | 175 | 15.9 | |

2010 speeds for control regions (outside, primed element numbers) were removed from measured 2010 landslide speeds. "landslide" and "outside" speeds are averages of kinematic element and control region speeds, respectively.

speed of 2.1 mm d⁻¹ (Table 1). The coefficient of determination for a linear fit between distance to control region centroids and speed was 0.44 for all regions and 0.88 if region 1011' was omitted. We considered this apparent movement of regions outside of the landslide to reflect systematic error in the measurements, so we removed the survey-long control region speeds from the corresponding kinematic element speeds (Table 1, Fig. 5). The resulting element speeds display relative relations similar to those from 1985 to 1990 but were lower, ranging between 0.4 and 7.8 mm d⁻¹.

The average number of measurements per kinematic element and scan ranged from 55 to 6164 and averaged 2609 for all elements; however, the measurement count for element 10 (55) was anomalously low because it was obscured by topography and the next lowest measurement count was 658 (element 3, Table 1). The average number of measurements per control region and scan ranged from 57 to 3350 and averaged 724 for all regions; some measurements were shared between overlapping control regions (Fig. 6). The standard deviations of speeds measured within kinematic elements ranged from 2.5 to 17.8 mm d⁻¹ and were similar for control regions (1.1–15.9 mm d⁻¹; Table 1).

Standard deviations displayed correlation with the number of point measurements (Fig. 7), especially for control regions, with standard deviation decreasing with increasing number of measurements. Variations between individual measurements often occurred over distances of only several meters, including within a given element/region (Fig. 6; Schulz et al., 2012). The spatiotemporal variability of individual point measurements is highlighted by Fig. 8, which shows example displacement time series for four kinematic elements. Average displacements of all points within each kinematic element and corresponding control region are shown, as well as displacements of one point within each element and region. These points were selected randomly from points for which cumulative displacement for the full survey period was within 0.5 mm of the average cumulative displacement for the respective element or region. Table 2 provides the average displacements for all kinematic elements and control regions, and also cumulative displacements measured using GPS and extensometers.

Averages of all measurements from the landslide indicated that its speed varied during the survey period from -0.2 to 0.9 mm h⁻¹ and averaged 0.2 mm h⁻¹, while the averages from outside of the landslide (control regions) indicated apparent speeds that ranged between -0.1 and 0.2 mm h⁻¹ (Fig. 9) with an average of 0.0 mm h⁻¹. Results suggest that speed of the entire landslide generally varied on a several-hour basis as cycles of acceleration and deceleration (Fig. 9). The landslide apparently moved more rapidly than 0.4 mm h⁻¹ seven times during the survey, mostly in the absence of marked speed increases in the control regions, and stopped moving (speed ≤ 0 mm h⁻¹) five times during the survey. Four of these periods of apparent stoppage (at ~49, 51, 61, and 103 elapsed hours) persisted for just one hourly measurement while the fifth period (~93–95 elapsed hours) persisted for three hourly measurements.

Fig. 10 shows speeds of three areas inside and outside of the landslide for the duration of the survey. To improve the signal-to-noise ratio and clarity of the figure, we first applied a low-pass filter to average speeds of each kinematic element and control region using a 3-period window and then averaged results for elements located in similar parts of the landslide and for adjacent control regions. The kinematic elements whose speeds are shown (4–5, 6–7, and 8–9; Fig. 10) provide a view of the distribution of speed along the length of the landslide for faster-moving areas.

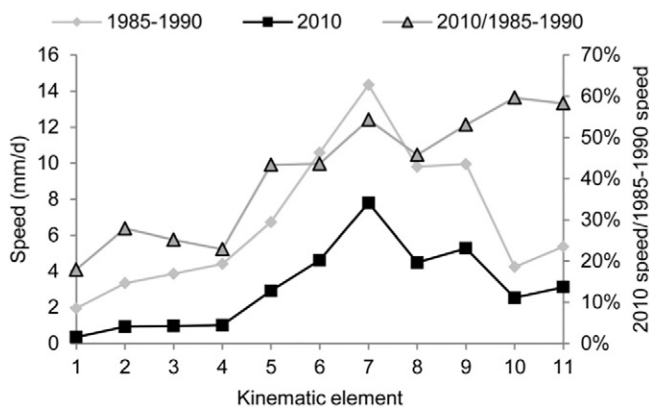


Fig. 5. Average speeds of the kinematic elements during Aug. 1985–Aug. 1990 and during the 2010 GBInSAR survey. The ratios of 2010 to 1985–1990 speeds are also shown (in terms of percentage).

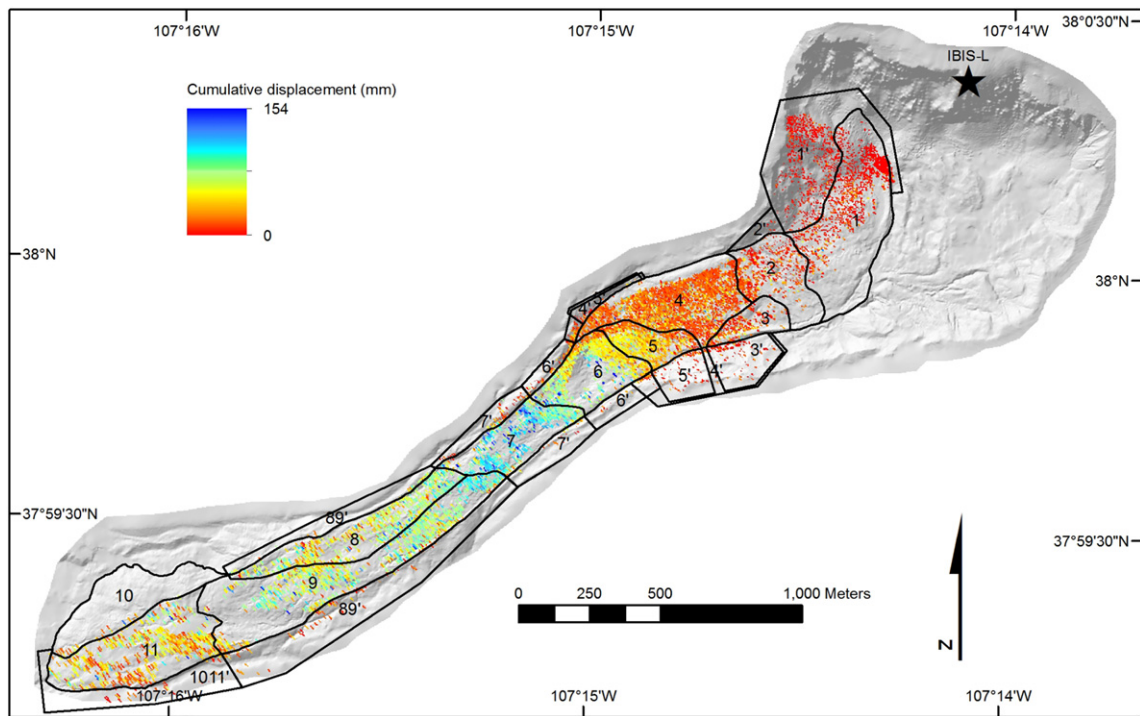


Fig. 6. Map showing cumulative displacements measured during the GBInSAR survey. Also shown are kinematic elements delineated from 1985 to 1993 data (Smith, 1993; Fleming et al., 1999) and control regions outside of the landslide adjacent to the elements in which InSAR measurements were obtained.

4.3. Long-term meteorology

Fig. 11 indicates that the annual average air temperature near the landslide increased at a rate of $0.07\text{ }^{\circ}\text{C year}^{-1}$ (coefficient of determination of 0.51) from water year 1983 to water year 2009 (water years begin Oct. 1 and end Sept. 30), while annual cumulative precipitation decreased between water years 1981 and 2009 by an average of 3.5 mm year^{-1} (Fig. 11). The precipitation decrease was unsteady, with a linear trend displaying a coefficient of determination of just 0.06.

5. Discussion

5.1. The ability of GBInSAR to quantify kinematics

The IBIS-L revealed a spatial distribution of the landslide's kinematics very similar to that revealed by the previous long-term studies that

utilized traditional approaches (Figs. 5 and 6; Smith, 1993; Fleming et al., 1999), and this revelation was complete within less than one day (Schulz et al., 2012). Hence, with a few days of effort, GBInSAR revealed kinematics with greater spatial coverage than Smith (1993) and with nearly continuous temporal coverage for the defined duration of the survey period. However, although relative motions between kinematic elements were revealed by the GBInSAR, structural conditions can only be revealed by detailed mapping such as that performed by Fleming et al. (1999), and such mapping also best defines element boundaries, especially where InSAR data are sparse and speed variations between elements are small. Additionally, error of GBInSAR measurements is somewhat ambiguous, as discussed below, and many individual pixel measures were almost certainly erroneous.

Close inspection of GBInSAR survey results indicates that measured displacements occasionally varied by up to two orders of magnitude over distances of meters (e.g., Fig. 6; also Fig. 8 in Schulz et al., 2012). Somewhat similarly, individual point measurements indicated uphill movement in some cases, which we believe was nearly always erroneous (e.g., element 11 point movement after ~65 h, Fig. 8). Much of the variable motion of individual points is almost certainly due to radar returns from unstable objects such as trees, while some is almost certainly real. It is reasonable to expect motion of the landslide to temporally vary on the order of millimeters to a few centimeters over distances of meters considering that zones of extension, compression, fracturing, and faulting are pervasive. Variable motion may occur from episodic movement along internal faults and folds, and of superficial failures that are numerous on the landslide's surface. We therefore expect that the observed variability in spatiotemporal motion at given point locations and within individual kinematic elements is real in some cases and erroneous in others due to returns from unstable objects; unfortunately, we cannot differentiate the two because we have no absolute knowledge of the landslide's motion. In contrast with point measurements, average displacements for kinematic elements generally agreed with displacements measured by extensometers (InSAR displacements were 102–113% of extensometer displacements; Table 2). Displacements derived from InSAR and GPS measurements did

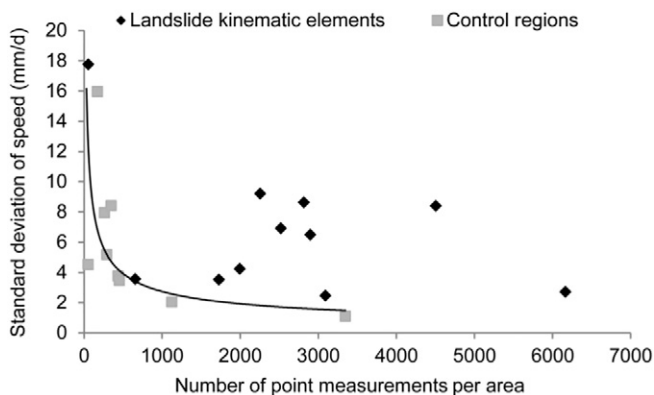


Fig. 7. Chart showing standard deviation of speeds versus the number of point measurements for given areas. The best-fit power-law regression for control regions is shown and has a coefficient of determination of 0.54.

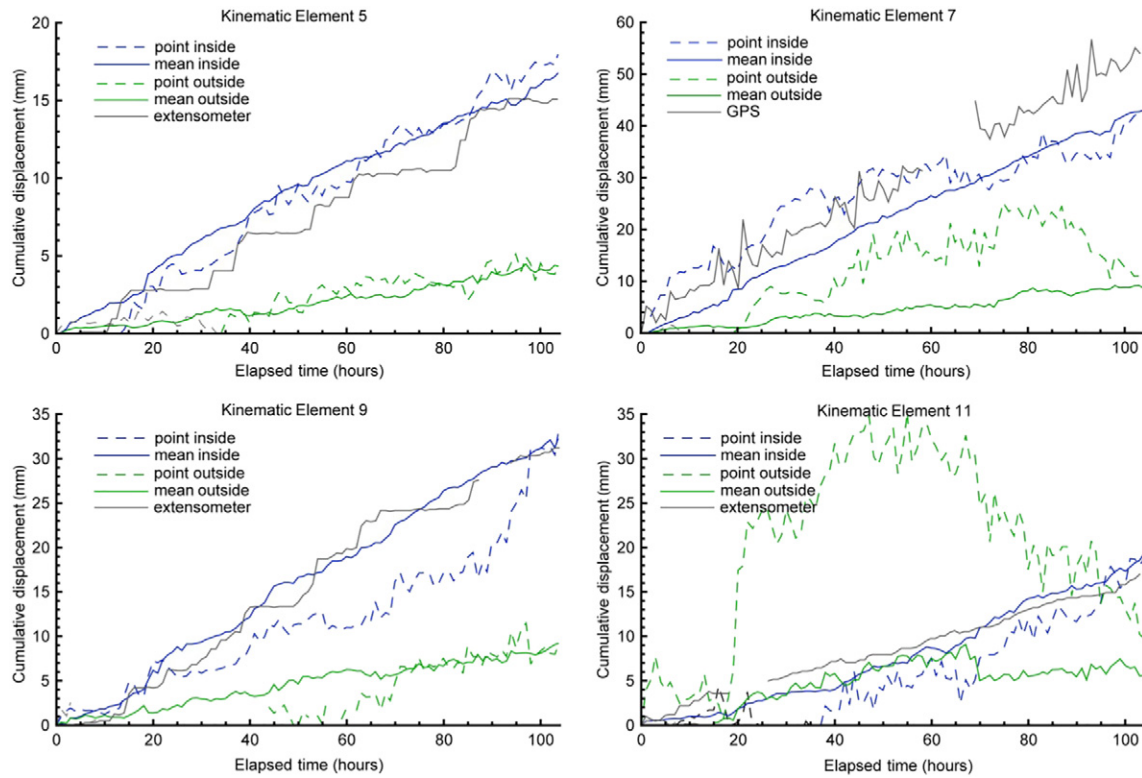


Fig. 8. Chart showing time series of displacements measured using InSAR, GPS surveying, and/or extensometers. Each panel shows results for a given kinematic element and the adjacent control region, including for a randomly selected InSAR data point, the mean of all InSAR data points in the given area, and results from in situ instrumentation.

not agree well in most cases (InSAR displacements were -81 – 178% of GPS displacements; Table 2), likely due to the ± 15 mm accuracy of GPS measurements being ~ 0.3 – 6 times cumulative displacements measured by InSAR and extensometers. The low accuracy of GPS results relative to actual landslide movement is highlighted by apparent uphill movement of three GPS monuments during the 4.3-day duration of the survey.

Although we cannot fully assess the accuracy of InSAR point measurements, averages of InSAR measurements provide some suggestions

of resolution and accuracy. The average speed of points outside of the landslide ranged from -0.1 to 0.2 mm h^{-1} and averaged 0.0 mm h^{-1} for the full survey period, which suggests positional accuracy for each scan on the order of ± 0.2 mm or better. This range agrees with the -0.2 – 0.9 mm range of average hourly landslide movement indicated by the InSAR results (overall speed average of 0.2 mm h^{-1}). However, error may have been more significant during some periods. For example, InSAR results indicated overall uphill-directed movement of the landslide as fast as -0.2 mm h^{-1} at ~ 93 – 95 elapsed hours, which we believe was erroneous; the landslide did not move uphill. With respect to motion resolution using averages of point measurements, hourly displacements on the order of 0.2 mm and higher were indicated associated with rainfall events at ~ 16 , ~ 19 and ~ 43 elapsed hours in the absence of similar movement of control regions outside of the landslide (Fig. 9), so were likely real. Other times absent clear potential triggers also displayed temporally variable landslide motion that did not correlate with motion of the control regions, including many such hourly variations of 0.1 – 0.3 mm. Hence, when individual point measurements are averaged over the landslide or control area, accuracy of ± 0.2 mm or better is generally suggested with resolution on the order of 0.1 mm, but periods of substantially decreased accuracy and resolution also may be present, so results must be evaluated with caution. It is likely that GBInSAR accuracy could be increased significantly with improved ability to identify and remove measurements from poor reflectors (e.g., trees), and from greater distribution and number of high-quality measurements obtained from non-moving ground.

The above discussion neglects the observation that control regions moved downhill during the survey and increasingly so with increased distance from the IBIS-L (Table 1). Because the relation between apparent movement and distance from the IBIS-L is approximately linear, we expect that differential settling of the apparatus occurred during the survey. Differential settling of just 0.001 mm would result in the observed pattern of increasing movement with distance from the IBIS-L.

Table 2
Results from displacement monitoring.

| Kinematic element | GPS monument | Extensometer | Total displacement (mm) | | |
|-------------------|--------------|--------------|-------------------------|---------|--------------|
| | | | InSAR | GPS | Extensometer |
| 1 | MP2 | | 2.6 | -6.6 | |
| 2 | MP5 | | 5.5 | -10.4 | |
| 3 | MP4 | | 6.5 | 18.9 | |
| 4 | MP3 | | 7.9 | 9.5 | |
| 4 | MP6 | | 6.0 | -7.4 | |
| 5 | | Upper | 17.0 | | 15.1 |
| 6 | MP8 | | 20.2 | 35.5 | |
| 6 | MP9 | | 20.1 | 52.4 | |
| 7 | MP10 | | 32.1 | 23.4 | |
| 7 | MP12 | | 32.7 | 26.8 | |
| 7 | MP21 | | 42.4 | 54.0 | |
| 8 | MP13 | | 20.4 | 17.3 | |
| 9 | MP14 | | 24.2 | 19.6 | |
| 9 | | Middle | 31.9 | | 31.2 |
| 11 | | Lower | 19.1 | | 17.0 |
| 11 | MP16 | | 18.7 | 10.5 | |
| 11 | MP19 | | 14.6 | 13.8 | |

InSAR displacements are for time intervals similar (± 0.5 h) to those for GPS displacements.

GPS and extensometer displacements are relative to the IBIS-L planimetric line of sight; negative values indicate motion toward the IBIS-L.

Middle and lower extensometer displacements include offsets (see text).

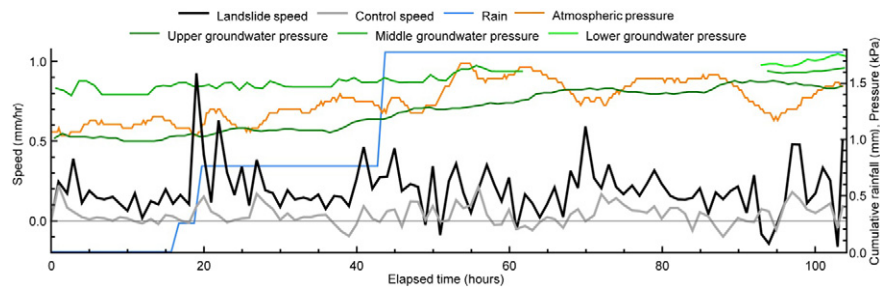


Fig. 9. Chart showing speeds of the landslide and control region. Also shown are cumulative rainfall, atmospheric pressure, and groundwater pressures; pressures are offset by arbitrary constants to improve figure clarity.

5.2. Long-term kinematics and potential controls

Using the average speeds for 1985–1990, the landslide moved ~20–130 m between 1985 and 2010. Even with this amount of movement, the kinematic element boundaries that may be inferred from the InSAR data generally appeared to have been consistent between these times and overall block-like motion of each element persisted (Fig. 6). Additionally, relative motion between elements was similar (but with important differences discussed below) during 1985–1990 and 2010 (Fig. 5). Hence, it is likely that the landslide's basal boundary geometry remained spatially consistent as it largely controls internal landslide kinematics (e.g., Baum et al., 1993, 1998; Fleming et al., 1999; Coe et al., 2009).

Although the distribution of kinematic variation across the landslide appeared grossly similar during 1985–1990 and 2010, the landslide moved more slowly during 2010 at 47% of the earlier speed and the speed decrease varied by kinematic element (Table 1, Fig. 5). Speeds of elements 1–4 during 2010 were just 18–28% of 1985–1990 speeds, while elements 5–11 moved during 2010 at 43–60% of 1985–1990 speeds. It is unlikely that these variations resulted from seasonal factors because extensometers indicated that the landslide was moving at 97–103% of the 2010 annual average speed during the 4.3-day InSAR survey (97% for the upper and lower extensometers and 103% for the middle extensometer; Schulz et al., 2012). This suggests that the InSAR survey results well represent annual average displacement. Therefore, the significantly different overall speed and speed distribution must have resulted from long-term changes that occurred between about 1985 and

2010. Assuming infinite-slope conditions and slope-parallel groundwater flow, the Coulomb failure rule (e.g., Lambe and Whitman, 1969) considering nil cohesion (valid for existing shear surfaces, e.g., Terzaghi et al., 1996) and Newton's second law of motion indicate that landslide acceleration is given by:

$$a = g \sin\theta - g \tan\phi \cos\theta \left(1 - \frac{s\rho_w}{s\rho_s + u\rho_u} \right) \quad (1)$$

where g is gravitational acceleration, θ is the inclination of the ground surface, water table, and landslide base, ϕ is the angle of internal friction of the landslide base, ρ_w , ρ_s , and ρ_u are mass densities of water and landslide material below and above the water table, respectively, and s and u are the slope-normal thicknesses of landslide material below and above the water table, respectively. Eq. (1) indicates that s and u control landslide acceleration by modulating frictional resistance of the landslide base. For constant landslide thickness, a rising water table (increasing s and decreasing u) results in increasing acceleration with the opposite true for a falling water table. Landslide thickness may vary through addition or removal of material; however, it also varies above fixed locations along the landslide base as material of variable thickness slides past. Assuming a stationary water table (constant s), decreasing thickness (u) results in landslide acceleration and increasing thickness results in deceleration for infinite-slope conditions. Below, we examine whether variations in landslide thickness or groundwater levels may have been responsible for the observed changes in landslide kinematics.

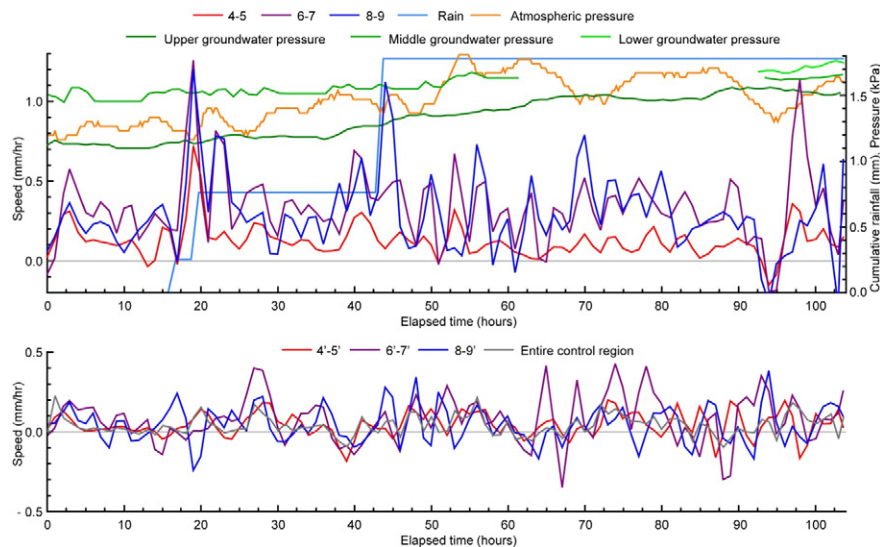


Fig. 10. Chart showing speeds of several areas of the landslide and adjacent control regions. Also shown are cumulative rainfall, atmospheric pressure, and pore-water pressures. Speeds are averaged for the kinematic elements and control regions shown. Pressures are offset by arbitrary constants to improve figure clarity. Speeds were smoothed using a 3-period low-pass filter.

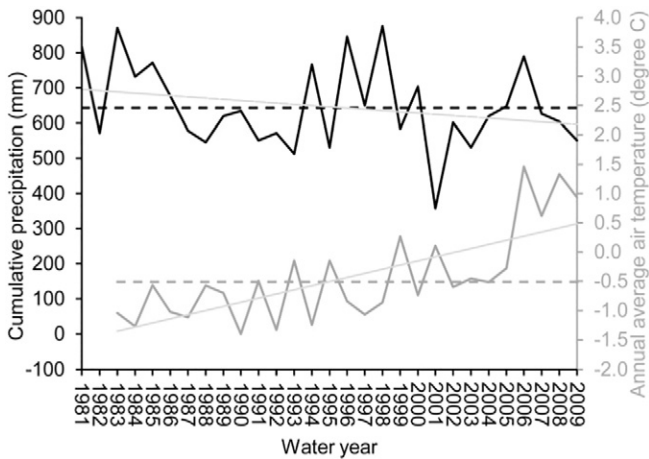


Fig. 11. Chart showing cumulative annual precipitation and annual average air temperature by water year. Water years cover October 1–September 30 and are named by the calendar year during which they commenced. Most data are from the Slumgullion SNOTEL station; air temperature data for parts of water years 1992–1994 are from the Beartown SNOTEL station and are offset by -0.35°C . Dashed lines show respective averages for the full period while light gray lines show linear best fits to the data.

5.2.1. Groundwater pressure

Similar to many landslides and in agreement with Eq. (1), speed of the Slumgullion landslide and parts thereof have been observed to directly correlate with changes in water-table position (e.g., Coe et al., 2003; Schulz et al., 2009a) and with the occurrence of rainfall and snowmelt in the absence of water-table observations (e.g., Fleming et al., 1999). It is well established that groundwater levels increase from infiltration of precipitation and decrease from evapotranspiration, which is largely controlled by air temperature (e.g., Hargreaves and Samani, 1982; Allen et al., 1998). Air temperature increased and precipitation decreased during the study period (Fig. 11), which likely resulted in reduced groundwater levels and landslide saturated thickness. This almost certainly contributed to the observed reduction of landslide speed (Eq. (1)). However, the observed differential slowing cannot be explained by overall drier and warmer conditions, so it seems likely that other factors contributed to the differential slowing.

5.2.2. Landslide geometry and kinematic element interaction

Changing thickness of landslide material can significantly affect landslide speed (e.g., Eq. (1)). Coe et al. (2009) analyzed aerial photographs from 1939, 1940, and 2000 and identified that the ground surface uphill approximately from the boundary between kinematic elements 5 and 6 was lower during 2000 by an average of 3.4 m. The landslide head probably moved ~40–315 m (using 1985–1990 speeds) between 1939/40 and 2000, which is insufficient to cause lowering over the ~1000-m-long region by sliding thinner material across the area. Additionally, Coe et al. (2009) found no region that thickened downslope. We suspect that lowering of the ground surface resulted from the head region sliding along a failure surface more steeply inclined than the ground surface because the landslide head displayed consistent lowering while areas downslope displayed similar topography (Coe et al., 2009); a steeper failure surface below a landslide head necessitates a listric geometry with a downslope region flatter than the ground surface. Evaluation of potential effects on landslide stability of subtly thinning, variably thick material sliding across a listric failure surface requires knowledge of landslide failure-surface geometry and analyses more complex than permitted by Eq. (1). We performed such an evaluation using estimated landslide geometry in two-dimensional slope-stability analyses, as described below.

We used results from semi-annual differential GPS surveys (Coe, 2012) of monuments on the upper part of the landslide (Fig. 2) to

infer topography of the landslide base by assuming that monument displacements were parallel to the base. We plotted each displacement time series on a topographic profile in its proper position along the ground surface (Fig. 12), then split each at its center and enlarged each half in the up- or downslope direction, as appropriate, until reaching the similarly treated enlargement of adjacent displacement time series. Beginning with MP2 and progressing in the downslope direction, the enlarged displacement time series were projected to an arbitrary depth and joined end to end to reveal potential orientation of the failure surface. As indicated on Fig. 12, this produced a smooth, arcuate failure surface that is steeper than the ground surface at its upslope end and gradually flattens from the upslope end of the head to the downslope end near and downslope from the kinematic element 5/6 boundary. The greater downslope inclination of the landslide base than of the ground surface explains Coe et al.'s (2009) observed thinning of the landslide head.

We analyzed changing stability of the landslide head resulting from its varying thickness following the generalized limit equilibrium (GLE) method-of-slices force- and moment-balance approach using a half-sine interslice force function (Fredlund and Krahn, 1977; Fredlund et al., 1981) and coded in Slide v.6 (Rocscience). Landslide geometry analyzed was based on the reconstructed landslide basal failure surface (Fig. 12) and topographic profiles developed from a 1985 digital elevation model (Powers et al., 1992) and 2011 aerial photographs. Arbitrarily selected material density and groundwater conditions were unchanged between the stability analyses and shear strength was initially calibrated using the 1985 profile so that the ratios of resisting to driving forces and moments were just less than unity, indicating instability. Analyses indicated a 1% increase in stability due to topographic change between 1985 and 2011. Additionally, analysis using Coe et al.'s (2009) 1939–1940 topographic profile indicated a 4% increase in stability of this region by 2011. Hence, sliding of a fixed volume of landslide material comprising Slumgullion's head likely occurred along a listric failure surface and at least partly caused the marked slowing of the head between 1985–1990 and 2010 (Fig. 5). Head movement imparts shear stress to downslope areas of a landslide so the gradual slowing of the head contributed to slowing of the overall landslide by reducing transferred shear stress; increasing tensile stress between the slowing head and more rapidly moving landslide downslope likely also contributed.

Stress changes at fixed locations above a landslide failure surface that result from variations in landslide total and/or saturated thickness control kinematics and may result in their spatiotemporal variability, as illustrated above. Comparison of Smith (1993) and Fleming et al. (1999) findings to the GBInSAR results suggests that kinematic boundary locations also may change. Speeds during 2010 abruptly changed within the northwestern parts of kinematic elements 5 and 6 about 30 m from their boundaries with element 4, rather than at the boundary itself as defined by previous work (Fig. 13). Similarly, 2010 speeds appear to have changed abruptly within the eastern part of element 5, rather than at the 4/5 boundary. The apparently different location of the downslope boundary of element 4 during 2010 could reflect error in the InSAR results or changes that occurred at the landslide between 1985–1990 and 2010. To evaluate these possibilities, we mapped faults in this region during 2011 assisted by GPS surveying and orthorectified aerial photographs (expected mapping positional accuracy of ± 1 m).

Our mapping (Fig. 13) indicated that fault characteristics and locations near the downslope end of kinematic element 4 substantially differed from those mapped by Fleming et al. (1999). The element 4/6 boundary and the western end of the 4/5 boundary comprised downslope-facing normal faults with oblique, right-lateral motion during 2011 located as much as 25 m downslope from the primarily upslope-facing normal faults and narrow shear zone with right-lateral motion that Fleming et al. (1999) mapped; their faults and shear zone in this area could not be found during 2011. Near the eastern part of the element 4/5 boundary within element 4, we observed that normal faulting

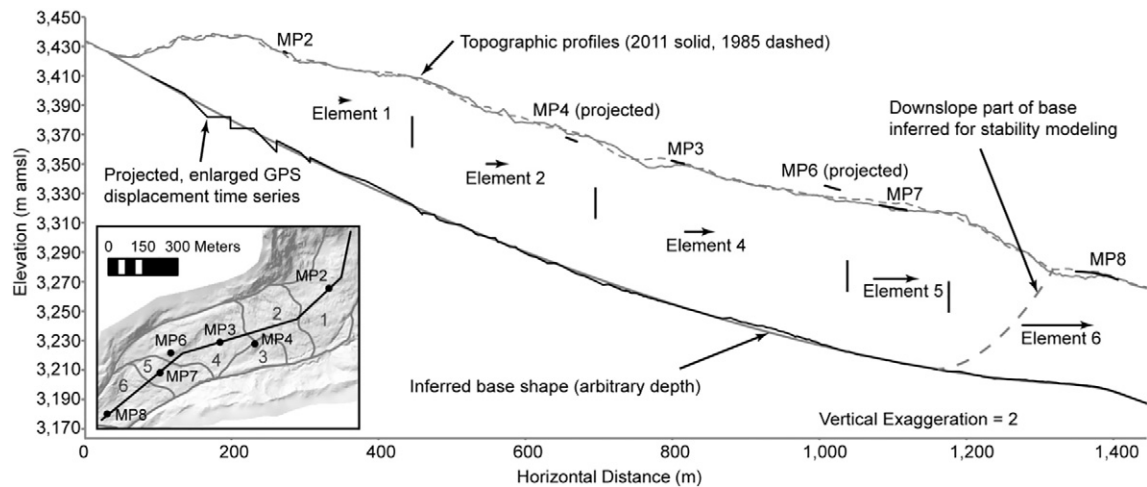


Fig. 12. Cross section of the landslide head with topographic profiles from 1985 and 2011. Inset map shows cross section location. MP# refers to GPS monitoring points with displacement profiles from Coe (2012) shown. The inferred basal failure surface is shown at an arbitrary depth as used during stability analyses. Arrows above the names of kinematic elements are 1985–2010 horizontal displacements estimated using speeds from Smith (1993) (Table 1).

extended just 10 m upslope from the boundary, rather than 30 m as mapped by Fleming et al. (1999). We also observed a normal fault with height reaching 5 m located approximately along the boundary where only a less-laterally extensive normal fault reaching 0.5 m high was mapped by Fleming et al. (1999). Additionally, we mapped a graben within element 5 ~40 m downslope from a similar graben mapped by Fleming et al. (1999). Finally, near the central part of the element 4 downslope boundary, we observed that the upslope limit of normal faulting during 2011 was as much as ~20 m downslope from the upslope limit mapped by Fleming et al. (1999). The fault locations that we observed during 2011 correlate with the abrupt speed changes between the elements revealed by the 2010 GBInSAR survey, suggesting that the survey results were not erroneous but instead helped to reveal evolving kinematics of the landslide. The 2011 fault characteristics are consistent with accelerated relative downslope movement at the boundary that likely results from the slower movement of the stabilizing head. It appears that the landslide may be forming a new head comprising element 5 and part of element 6 while abandoning elements 1–4.

5.3. Short-term kinematics and potential controls

Although accuracy of the GBInSAR survey results remains somewhat ambiguous, apparent motion of the control area suggests measurement accuracy on the order of ± 0.2 mm when point measurements are averaged. Landslide speed apparently varied by >0.2 mm h⁻¹ multiple

times during the survey (Fig. 9), but there also were periods where variability was <0.2 mm h⁻¹. Below, we discuss apparent characteristics of landslide motion with magnitudes similar to potential error so we note the caveat that some characteristics of apparent motion described herein may well be erroneous. Assuming that it is not due to error in InSAR results, unsteady motion of the landslide (Fig. 9) could reflect changes in forcing conditions, kinematic element interactions, and/or shear resistance of landslide boundaries. We evaluate these hypotheses below.

5.3.1. Rainfall and pressures

No consistent correlation is apparent between speed variations and observed pore-water pressures across multiple timescales during the GBInSAR survey (Fig. 9). Schulz et al. (2009b) observed that the landslide typically accelerated during atmospheric tidal lows, probably due to tidally induced pore-fluid movement altering effective normal stress and, hence, frictional stress at the landslide base. Atmospheric tides were apparent only during the last two days of the survey with peak low tides occurring at ~71 and 95 elapsed hours (Fig. 9). These low tides were accompanied by two of the seven periods of relatively rapid landslide movement in agreement with Schulz et al. (2009b); however, the extended period during which the landslide apparently stopped moving (~93–95 elapsed hours) also occurred during the second tidal low. Worth noting is that much of the processing required with InSAR is for removal of artifacts resulting from variations in atmospheric conditions (e.g., Bürgmann et al., 2000), although the control regions did not display apparent uphill movement during ~93–95 elapsed

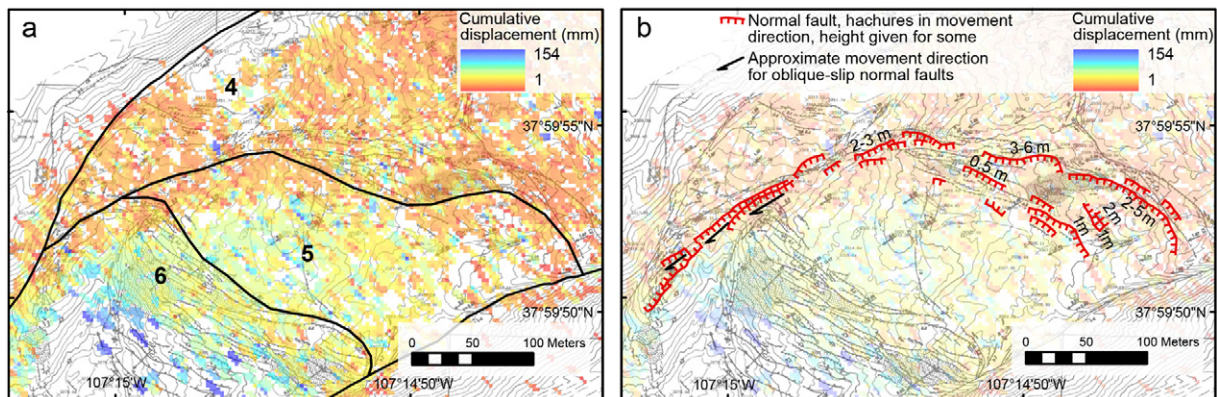


Fig. 13. Maps depicting conditions at the element 4/5/6 boundary. GBInSAR-derived cumulative displacements, kinematic element boundaries (panel a), and faults mapped during 2011 (panel b) underlain by the Fleming et al. (1999) structural map are shown.

hours. Our results suggest that apparent variations in landslide speed cannot be ascribed to observed changes in pore-water pressures, while speed may have increased due to upward pore-fluid movement and consequent reductions in basal frictional resistance during atmospheric tidal lows.

Although rainfall-induced pore-pressure changes were not apparent in our piezometer records (Fig. 9), infiltration of rainfall may increase pore-water pressures along landslide failure surfaces and cause landslide acceleration (Eq. (1)). Rainfall occurred three times during the GBInSAR survey and each time was closely associated with a period of relatively fast landslide movement. Rainfall events occurred at 15.7–16.7 and 18.7–19.7 elapsed hours, and the landslide accelerated at 18 and 21 h to speed peaks at 19 and 22 h. Hence, considering measurement timing, onset of landslide acceleration lagged behind the start of rainfall by 1.3–3.3 h for these two events. Similarly, rainfall occurred at 42.7–43.7 elapsed hours and the landslide accelerated at 44 h before reaching peak speed at 45 h; hence, the lag time between the onset of rainfall and landslide acceleration was 0.3–2.3 h. The time delays between rainfall and apparent landslide acceleration and the lack of consistent response of control regions to rainfall strongly suggest that the GBInSAR measurements reflect true landslide motion, and that accelerated motion resulted from the rainfall. Furthermore, the delays are consistent with some revealed by three years of monitoring performed at the landslide (Schulz et al., 2009a) and at other, similar landslides (e.g., Keefer and Johnson, 1983; Reid, 1994; Baum and Reid, 1995). However, these studies related significant landslide acceleration (faster periods lasting days to weeks) to significant precipitation events (multi-day to seasonal) while rainfall amounts during our study were seemingly negligible, with only 0.25, 0.51, and 1.02 mm falling during the first, second, and third events, respectively.

Although cumulative rainfall during any of the events intuitively may seem to have been insufficient to affect motion of the landslide, evidence suggests a connection, so further examination seems warranted. The water table within the landslide appears to be typically ~0–3 m below the ground surface (Coe et al., 2003; Schulz et al., 2007, 2009a), in agreement with our piezometer measurements that indicated groundwater depths during the survey of 0.6–2.1 m below ground surface. These shallow depths and the clayey nature of the landslide suggest that much of it was probably tension saturated to near the ground surface making it possible for infiltrating rainfall to directly transmit pore pressure increases through the unsaturated zone to the water table and below (e.g., Haneberg, 1991; Baum and Reid, 1995). Additionally, many ponds connected to the landslide's groundwater system and other regions of apparently full soil saturation exist at the landslide (e.g., Fleming et al., 1999; Coe et al., 2009), including along parts of the landslide's marginal strike-slip fault zones where surface water flow often concentrates (Parise et al., 1997). To provide a simple evaluation of potential pore-pressure response to the rainfall events, we assumed full saturation of landslide material and adapted a one-dimensional model for heat diffusion (Carslaw and Jaeger, 1959), also assuming that the landslide material is homogeneous and isotropic:

$$P(y, t) = P_0 \operatorname{erfc} \left(\frac{y}{2\sqrt{Dt}} \right) \quad (2)$$

where P is the pressure developed at given time t and depth y , D is hydraulic diffusivity of the landslide material, and P_0 represents an instantaneously and permanently applied change in pressure at the ground surface resulting from rainfall. Eq. (2) was used by Handwerger et al. (2013) to evaluate the initiation of landslide motion following the onset of seasonal rainfall, while others have used a solution to the linear diffusion equation that utilizes application of sinusoidally varying pressure or rainfall flux to evaluate landslide response to periodic rainstorms (e.g., Iverson and Major, 1987; Haneberg, 1991; Reid, 1994; Baum and Reid, 1995). Assuming $D = 7.8 \times 10^{-5} \text{ m}^2 \text{ s}^{-1}$ as determined for the Slumgullion landslide (Schulz et al., 2009b), Fig. 14 shows model

results and suggests that meaningful pore-pressure increases would not propagate below ~2 m depth during the observed time lag between rainfall and landslide response. Fig. 14 also suggests that our shallowest piezometer (depth of 4.57 m) should not have revealed a pressure response, which agrees with observations. Schulz et al. (2009a) found strong evidence indicating that pore-water pressures along at least part of the landslide's marginal strike-slip faults affect motion of the landslide. From seismic and geodetic monitoring, Gombert et al. (2011) also concluded that the landslide's marginal faults played an important role in controlling motion of the landslide. Hence, it seems reasonable to infer that the seemingly negligible rainfall events triggered accelerated landslide motion by increasing shallow pore-water pressures and consequently decreasing frictional strength along the landslide's marginal strike-slip faults.

5.3.2. Shear resistance and kinematic element interaction

Although rainfall and low atmospheric tides may have been responsible for some of the observed variability in landslide speed, these forcing conditions cannot explain all variability. Additionally, the apparent reaction of the landslide to rainfall was opposite to what might be expected; faster movement occurred following lesser rainfall and vice versa (Fig. 9). Some of this ambiguity may result from error in InSAR results and spatial variability of rainfall across the large landslide. We hypothesize that much of the ambiguity results from changing resistance along the landslide's shear boundaries. Shear resistance that increases with shear rate is considered necessary for long-term persistent landslide motion (e.g., Terzaghi, 1931; Keefer and Johnson, 1983; Vulliet and Hutter, 1988; Baum and Johnson, 1993; Cross, 2005). Potential mechanisms resulting in resistance increasing with shear displacement rate include forced circulation of pore-water from deforming landslide debris sliding along asperities (Keefer and Johnson, 1983; Baum and Johnson, 1993; van Asch et al., 2007), shear-induced dilation and consequent reduction of pore-water pressure (e.g., Reynolds, 1885; Casagrande, 1936; Iverson et al., 1997, 2000; Moore and Iverson, 2002; Iverson, 2005), which apparently occurs at the Slumgullion landslide (Schulz et al., 2007, 2009a), and increased misalignment of shear-zone particles (e.g., Bishop et al., 1971; Lupini et al., 1981; Skempton, 1985; Tika et al., 1996; Wang et al., 2010; Schulz and Wang, 2014). Each of these mechanisms can produce unsteady motion, with surges of higher speed causing increased shear resistance and deceleration, while periods of lower speed (or no motion) permit positive pore-pressure recovery and alignment of shear-zone particles, both of which result in weakening. Additionally, similar to our long-term results that indicate the importance of changing stability of the landslide head affecting kinematics therein and also downslope, we hypothesize that

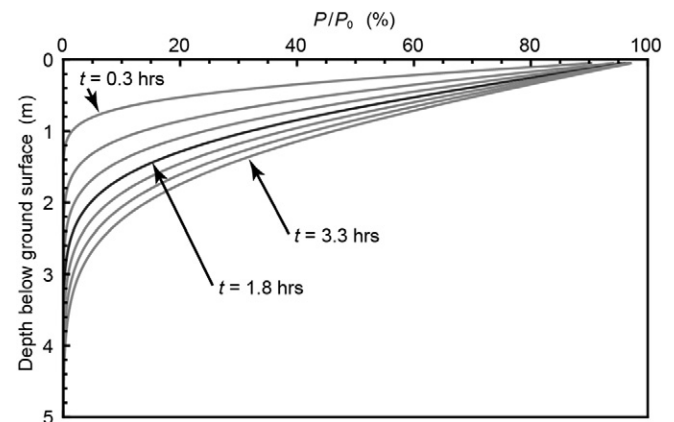


Fig. 14. Results from modeling pore-pressure response to rainfall. Each line represents the percentage of pressure transmitted from the ground surface to depth at a given time after pressure was first applied. Considering measurement frequency and timing, the landslide accelerated sometime between 0.3 and 3.3 h following the onset of each rainfall event.

short-term variability in stress transfer from differential motion of the kinematic elements also contributed to their variable motion and that of the landslide as a whole. The importance of the interaction of kinematic elements is well known for many phenomena from field and laboratory observations and modeling efforts. However, our observations (Fig. 10) suggest that kinematic element interaction is important even for sub-millimeter displacements occurring on an hourly basis across distances of kilometers.

As with movement of the landslide overall (Fig. 9), results suggested that movement of parts of the landslide also was cyclic (Fig. 10). Worth noting is that control region average speeds on Fig. 10 are especially noisy because they result from relatively small numbers of point measurements (352–1586); noise is reduced as the number of point measurements increases (Fig. 7). During some periods, cyclic movement was generally in phase for the different parts of the landslide and peak speeds were relatively low. For example (Fig. 10), prior to the first rainfall event, speeds of the upper (elements 4 and 5), middle (elements 6 and 7), and lower (elements 8 and 9) parts of the landslide were slow and steady relative to most other periods and the general distribution of speeds was mostly in agreement with long-term averages, with speed being lowest in the upper part of the landslide, faster in the lower part, and fastest in the middle of the landslide. After the rainfall occurred, all parts of the landslide synchronously accelerated and reached their highest speeds of the survey period, even though this rainfall was the lowest of the three events. It may be that the previous, relatively steady movement with the different areas of the landslide moving at rates proportionally similar to their long-term averages resulted in shear stresses also being distributed along the length of the landslide similarly to long-term averages, which aided the synchronous, rapid movement. This rapid movement surge likely increased resistance along the landslide's shear boundaries. During the second, larger rainfall event that immediately followed, the upper part of the landslide showed little reaction and the middle and lower parts of the landslide again surged downslope, but at lower speeds than after the first, smaller rainfall event. The reduced response may be explained by the increased shear resistance and the lack of movement of the upper part of the landslide; hence, it transferred no driving shear stress to the landslide downslope and increased tensile stresses likely developed between the areas, helping to slow the middle and lower parts of the slide mass.

Following the first two rainfall events, all parts of the landslide resumed their relatively steady, slow movement until ~38–42 elapsed hours when a pulse of higher speed occurred. After this pulse, the third, largest rainfall event occurred and was followed by very rapid movement of the lower part of the landslide that persisted for ~3 h. The middle part of the landslide accelerated ~1 h after the lower part, while the upper part barely responded. We expect that the fast pulse of motion prior to the rainfall again likely caused resistance of shear boundaries to increase, so contributed to the relatively small reaction of the upper and middle parts of the landslide, but it is unclear why movement of the lower part of the landslide was anomalously high. One explanation could be spatial variability of rainfall as we have often observed during field visits to the landslide, but no measurements are available to support this hypothesis.

Motion of the various parts of the landslide was relatively unsteady for ~18 h (to ~66 elapsed hours) after the response to the third rainfall event, with periods generally ~4 h long of rapid motion separated by very slow movement or stoppage. Additionally, relative speeds varied and some parts of the landslide often did not move synchronously with the other parts. For example, the lower part barely moved at ~52–55 elapsed hours while the middle and upper parts moved rapidly. The reduced movement of the lower part probably partly resulted from its anomalously rapid motion following the third rainfall event, which likely increased resistance of its bounding shear zones. Additionally, its relatively great previous motion should have reduced shear stress imparted by upslope material and increased tensile stress between the areas, which also would contribute to its subsequent slowing.

Immediately after this period of very slow movement of the lower part (~52–54 elapsed hours), it again surged downslope faster than the other areas (~54–58 elapsed hours), likely at least partly due to increased shear stresses from the preceding movement of upslope areas and weakening of bounding shear zones during its previous slow movement.

After ~66 elapsed hours and until ~92 elapsed hours, the landslide moved at a relatively fast and steady rate, presumably because motion and stress transfer became more organized; that is, motion of individual parts of the landslide gradually reached their background averages after the disruptive, rapid surge of the lower part of the landslide that occurred after the third rainfall event. The distribution of speeds was not always steady, though; variable speed propagating along the landslide length was also suggested during this period. For example, motion was restricted to the middle and lower parts of the landslide at ~75–77 elapsed hours, which likely resulted in the surge of the upper part at ~77–80 h; this surge and one of the lower part at ~78–82 h probably aided a surge of the middle part of the landslide at ~81–85 h.

We cannot explain the apparent uphill motion of the landslide during ~93–95 elapsed hours. If the landslide in fact stopped, one explanation could be that the relatively long period of fast motion that preceded this period sufficiently increased resistance along the landslide's shear boundaries. The resistance should decay with time during periods of slow movement or stoppage. This decrease in resistance, along with decreased resistance from the concurrent low atmospheric tide, may have contributed to the markedly fast movement that ensued during ~95–102 elapsed hours.

6. Conclusion

We utilized traditional and emerging tools for measuring landslide kinematics to evaluate motion, its evolution, and potential controls thereon of the well-studied Slumgullion landslide. These tools included field mapping and photogrammetric displacement measurements from the 1980s and 1990s (Smith, 1993; Fleming et al., 1999), and deployment of a GBInSAR system to measure hourly ground-surface displacement during 2010. We found that spatial averages of InSAR-derived displacements were comparable to those from in situ measurements; InSAR results were apparently accurate within $\pm 0.2 \text{ mm h}^{-1}$ when more than ~1000 individual point measurements were averaged. The InSAR results generally revealed the landslide's kinematic elements that were delineated independently, and did so after only a few hours. However, structural relations between kinematic elements and locations of element boundaries remain best revealed by detailed field mapping.

Our results indicated that the landslide slowed by 2010 to about half its 1985–1990 speed and this slowing was greatest at the landslide head. Overall slowing was likely at least partly due to reduced pore-water pressures along the landslide's shear boundaries resulting from long-term air-temperature increase and precipitation decrease. Modeling suggested that observed thinning of the landslide head (Coe et al., 2009) caused its stability to increase, which resulted in its marked slowing. Slowing of the head should have aided overall slowing of the landslide by decreasing downslope-directed transfer of shear stresses. InSAR measurements suggested that similar changes, although with seemingly negligible magnitudes, also controlled short-term landslide movement. For example, the landslide apparently accelerated within a few hours of seemingly negligible rainfall, and pore-pressure diffusion modeling suggested that the acceleration resulted from pressure-induced weakening only of shallow parts of the landslide's marginal strike-slip faults. Additionally, InSAR results suggested that motion often propagated across kilometers from one area of the landslide to another, even following sub-millimeter displacements. Such motion induced by stress transfer was apparently modulated by the landslide's boundary shear resistance varying with shear displacement rate.

Acknowledgements

We thank Paolo Farina (formerly with IDS), Giorgio Barsachi (IDS), Patrick Miller (Olson Engineering), and Eric Jones, Jason Kean, and David Worley (USGS) for their assistance during this study. We thank Takashi Oguchi, Mario Parise, and Francis Rengers for their constructive reviews that improved this paper. The use of trade, product, industry, or firm names is for descriptive purposes only and does not imply endorsement by the U.S. Government. This research was funded by the U.S. Geological Survey Landslide Hazards program and IDS Corporation. Data obtained during this study are available from Schulz et al., 2016.

References

- Allen, R.G., Pereira, L.S., Raes, D., Smith, M., 1998. Crop evapotranspiration: guidelines for computing crop water requirements. FAO Irrigation and Drainage Paper 56. 300(9). Food and Agriculture Organization of the United Nations, Rome (D05109).
- Antonello, G., Casaglini, N., Farina, P., Leva, D., Nico, G., Sieber, A.J., Tarchi, D., 2004. Ground-based SAR interferometry for monitoring mass movements. *Landslides* 1, 21–28.
- Aryal, A., Brooks, B.A., Reid, M.E., Bawden, G.W., Pawlak, G.R., 2012. Displacement fields from point cloud data: application of particle image velocimetry to landslide geodesy. *J. Geophys. Res.* 117, F01029. <http://dx.doi.org/10.1029/2011JF002161>.
- van Asch, Th.W.J., Van Beek, L.P.H., Bogaard, T.A., 2007. Problems in predicting the mobility of slow-moving landslides. *Eng. Geol.* 91, 46–55.
- Baldi, P., Cenni, N., Fabris, M., Zanutta, A., 2008. Kinematics of a landslide derived from archival photogrammetry and GPS data. *Geomorphology* 102, 435–444.
- Barla, G., Antolini, F., Barla, M., Mensi, E., Piovano, G., 2010. Monitoring of the Beauregard landslide (Aosta Valley, Italy) using advanced and conventional techniques. *Eng. Geol.* 116, 218–235.
- Baum, R.L., Johnson, A.M., 1993. Steady movement of landslides in fine-grained soils – a model for sliding over an irregular slip surface. *U.S. Geological Survey Bulletin* 1842-D (Denver, CO).
- Baum, R.L., Reid, M.E., 1995. Geology, hydrology, and mechanics of a slow-moving, clay-rich landslide, Honolulu, Hawaii. In: Haneberg, W.C., Anderson, S.A. (Eds.), *Reviews in Engineering Geology X. Geological Society of America, Boulder, CO*, pp. 79–106.
- Baum, R.L., Fleming, R.W., Johnson, A.M., 1993. Kinematics of the Aspen Grove landslide, Ephraim Canyon, Central Utah. *U.S. Geological Survey Bulletin* 1842-F (Reston, VA).
- Baum, R.L., Messerich, J., Fleming, R.W., 1998. Surface deformation as a guide to kinematics and three-dimensional shape of slow-moving, clay-rich landslides, Honolulu, Hawaii. *Environ. Eng. Geosci.* 4 (3), 283–306.
- Bishop, A.W., Green, G.E., Garga, V.K., Andresen, A., Brown, J.D., 1971. A new ring shear apparatus and its application to the measurement of residual strength. *Geotechnique* 21 (4), 273–328.
- Burbank, D.W., Leland, J., Fielding, E., Anderson, R.S., Brozovic, N., Reid, M.R., Duncan, C., 1996. Bedrock incision, rock uplift and threshold hillslopes in the northwestern Himalayas. *Nature* 379, 505–510.
- Bürgmann, R., Rosen, P.A., Fielding, E.J., 2000. Synthetic aperture radar interferometry to measure Earth's surface topography and its deformation. *Annu. Rev. Earth Planet. Sci.* 28, 169–209.
- Calabro, M.D., Schmidt, D.A., Roering, J.J., 2010. An examination of seasonal deformation at the Portuguese Bend landslide, southern California, using radar interferometry. *J. Geophys. Res.* 115, F02020. <http://dx.doi.org/10.1029/2009JF001314>.
- Carslaw, H.S., Jaeger, J.C., 1959. *Conduction of Heat in Solids*. Oxford University Press, New York, NY.
- Casaglini, N., Catani, F., Del Ventisette, C., Luzi, G., 2010. Monitoring, prediction, and early warning using ground-based radar interferometry. *Landslides* 7:291–301. <http://dx.doi.org/10.1007/s10346-010-0215-y>.
- Casagrande, A., 1936. Characteristics of cohesionless soils affecting the stability of slopes and earth fills. *J. Boston Soc. Civil Eng.* 23 (1), 13–32.
- Cascini, L., Fornaro, G., Peduto, D., 2010. Advanced low- and full-resolution DInSAR map generation for slow-moving landslide analysis at different scales. *Eng. Geol.* 112, 29–42.
- Chleborad, A.F., Diehl, S.F., Cannon, S.H., 1996. Geotechnical properties of selected materials from the Slumgullion landslide. In: Varnes, D.J., Savage, W.Z. (Eds.), *The Slumgullion Earth Flow: A Large-scale Natural Laboratory*. U.S. Geological Survey Bulletin 2130, pp. 67–71 (Reston, VA).
- Coe, J.A., 2012. Regional moisture balance control of landslide motion: implications for landslide forecasting in a changing climate. *Geology* 40 (4):323–326. <http://dx.doi.org/10.1130/G32897.1>.
- Coe, J.A., Ellis, W.L., Godt, J.W., Savage, W.Z., Savage, J.E., Michael, J.A., Kibler, J.D., Powers, P.S., Lidke, D.J., Debray, S., 2003. Seasonal movement of the Slumgullion landslide determined from Global Positioning System surveys and field instrumentation, July 1998–March 2002. *Eng. Geol.* 68, 67–101.
- Coe, J.A., McKenna, J.P., Godt, J.W., Baum, R.L., 2009. Basal-topographic control of stationary ponds on a continuously moving landslide. *Earth Surf. Process. Landf.* 34: 264–279. <http://dx.doi.org/10.1002/esp.1721>.
- Coe, J.A., Baum, R.L., Allstadt, K.E., Kochevar Jr., B.F., Schmitt, R.G., Morgan, M.L., White, J.L., Stratton, B.T., Hayashi, T.A., Kean, J.W., 2016. Rock-avalanche dynamics revealed by large-scale field mapping and seismic signals at a highly mobile avalanche in the West Salt Creek valley, western Colorado. *Geosphere* 12 (2). <http://dx.doi.org/10.1130/GES01265.1>.
- Crandell, D.R., Varnes, D.J., 1961. Movement of the Slumgullion earthflow near Lake City, Colorado. *Short Papers in the Geologic and Hydrologic Sciences, U.S. Geological Survey Professional Paper* 424-B, pp. B136–B139.
- Cross, C.W., 1909. The Slumgullion mud flow. *Science* 30, 126–127.
- Cross, R., 2005. Increase in friction force with sliding speed. *Am. J. Phys.* 73 (9), 812–816.
- Cruden, D.M., Varnes, D.J., 1996. Landslide types and processes. In: Turner, A.K., Schuster, R.L. (Eds.), *Landslides, Investigation and Mitigation, Transportation Research Board Special Report* 247. National Research Council, Washington, D.C., pp. 36–75.
- Dehls, J., Giudici, D., Farina, P., Martin, D., Froese, C., 2010. Monitoring Turtle Mountain using ground-based synthetic aperture radar (GB-InSAR). *Proceedings of the 63rd International Canadian Geotechnical Conference and 6th Canadian Permafrost Conference*, Calgary, Alberta, 635–1640.
- Endlich, F.M., 1876. Report of F.M. Endlich. *U.S. Geological Survey of the Territories Annual Report* 1874, p. 203.
- Ferretti, A., Prati, C., Rocca, F., 2001. Permanent scatterers in SAR interferometry. *IEEE Trans. Geosci. Remote Sens.* 39, 8–20.
- Fleming, R.W., Johnson, A.M., 1989. Structures associated with strike-slip faults that bound landslide elements. *Eng. Geol.* 27, 39–114.
- Fleming, R.W., Baum, R.L., Giardino, M., 1999. Map and Description of the Active Part of the Slumgullion Landslide, Hinsdale County, Colorado. *U.S. Geological Survey Geologic Investigations Series Map* I-2672 (Reston, VA).
- Fredlund, D.G., Krahn, J., 1977. Comparison of slope stability methods of analysis. *Can. Geotech. J.* 14, 429–439.
- Fredlund, D.G., Krahn, J., Pufahl, D.E., 1981. The relationship between limit equilibrium slope stability methods. *Proceedings of the 10th International Conference on Soil Mechanics and Foundation Engineering*, Stockholm, Sweden. A.A. Balkema, Rotterdam, Netherlands, pp. 409–416.
- Gant, P.H., 1952. *The Case of Alferd Packer the Man-eater*. University of Denver Press, Denver, CO.
- Gentile, C., Bernardini, C., 2009. An interferometric radar for non-contact measurement of deflections on civil engineering structures: laboratory and full-scale tests. *Struct. Infrastruct. Eng.* 6 (5):521–534. <http://dx.doi.org/10.1080/15732470903068557>.
- Giordan, D., Allasia, P., Manconi, A., Baldo, M., Satangelo, M., Cardinali, M., Corazza, A., Albanese, V., Lollino, G., Guzzetti, F., 2013. Morphological and kinematic evolution of a large earthflow: the Montaguto landslide, southern Italy. *Geomorphology* 187: 61–79. <http://dx.doi.org/10.1016/j.geomorph.2012.12.035>.
- Gischig, V., Loew, S., Kos, A., Moore, J.R., Raetz, H., Lemy, F., 2009. Identification of active release planes using ground-based differential InSAR at the Randa rock slope instability, Switzerland. *Nat. Hazards Earth Syst. Sci.* 9, 1–12.
- Gomberg, J., Bodin, P., Savage, W., Jackson, M.E., 1995. Landslide faults and tectonic faults, analogs?: the Slumgullion earthflow, Colorado. *Geology* 23 (1), 41–44.
- Gomberg, J.S., Schulz, W.H., Bodin, P., Kean, J.W., 2011. Seismic and geodetic signatures of fault slip at the Slumgullion landslide natural laboratory. *J. Geophys. Res.* 116, B09404. <http://dx.doi.org/10.1029/2011JB008304>.
- Guerriero, L., Coe, J.A., Revellino, P., Grelle, G., Pinto, F., Guadagno, F.M., 2014. Influence of slip surface geometry on earth-flow deformation, Montaguto earth flow, southern Italy. *Geomorphology* 219:285–305. <http://dx.doi.org/10.1016/j.geomorph.2014.04.039>.
- Guzzi, R., Parise, M., 1992. Surface features and kinematics of the Slumgullion landslide, near Lake City, Colorado. *U.S. Geological Survey Open-file Report* 92-252 (Reston, VA).
- Handwerger, A.L., Roering, J.J., Schmidt, D.A., 2013. Controls on the seasonal deformation of slow-moving landslides. *Earth Planet. Sci. Lett.* 377–378:239–247. <http://dx.doi.org/10.1016/j.epsl.2013.06.047>.
- Handwerger, A.L., Roering, J.J., Schmidt, D.A., Rempel, A.W., 2015. Kinematics of earthflows in the Northern California Coast Ranges using satellite interferometry. *Geomorphology* 246:321–333. <http://dx.doi.org/10.1016/j.geomorph.2015.06.003>.
- Haneberg, W.C., 1991. Observation and analysis of pore pressure fluctuations in a thin coluvium landslide complex near Cincinnati, Ohio. *Eng. Geol.* 31, 159–184.
- Hargreaves, G.H., Samani, Z.A., 1982. Estimating potential evapotranspiration. *J. Irrig. Drain. Div.* 108 (3), 225–230.
- Hillel, G.E., Bürgmann, R., Ferretti, A., Novali, F., Rocca, F., 2004. Dynamics of slow-moving landslides from permanent scatterer analysis. *Science* 304, 1952–1954.
- Iverson, R.M., 2005. Regulation of landslide motion by dilatancy and pore pressure feedback. *J. Geophys. Res.* 110, F02015.
- Iverson, R.M., Major, J.J., 1987. Rainfall, ground-water flow, and seasonal movement at Minor Creek landslide, northwestern California: physical interpretation of empirical relations. *Geol. Soc. Am. Bull.* 99, 579–594.
- Iverson, R.M., Reid, M.E., LaHusen, R.G., 1997. Debris-flow mobilization from landslides. *Annu. Rev. Earth Planet. Sci.* 25, 85–138.
- Iverson, R.M., Reid, M.E., Iverson, N.R., Lahusen, R.G., Logan, M., Mann, J.E., Brien, D.L., 2000. Acute sensitivity of landslide rates to initial soil porosity. *Science* 290, 513–516.
- Jaboyedoff, M., Oppikofer, T., Abellan, A., Derron, M.-H., Loye, A., Metzger, R., Pedrazzini, A., 2012. Use of LIDAR in landslide investigations: a review. *Nat. Hazards* 61, 5–28.
- Keefer, D.K., Johnson, A.M., 1983. Earth flows: morphology, mobilization, and movement. *U.S. Geological Survey Professional Paper* 1264 (Reston, VA).
- Lambe, T.W., Whitman, R.V., 1969. *Soil Mechanics*. John Wiley & Sons, New York, NY.
- Lipman, P.W., 1976. Geologic map of the Lake City caldera area, western San Juan Mountains, southwestern Colorado. *U.S. Geological Survey Miscellaneous Investigation Series Map* I-962 (Reston, VA).
- Löve, D., 1970. Subarctic and subalpine: where and what? *Arct. Alp. Res.* 2 (1), 63–73.
- Lowry, B., Gomez, F., Zhou, W., Mooney, M.A., Held, B., Grasmick, J., 2013. High resolution displacement monitoring of a slow velocity landslide using ground based radar interferometry. *Eng. Geol.* 166, 160–169.
- Lupini, J.F., Skinner, A.E., Vaughan, P.R., 1981. The drained residual strength of cohesive soils. *Geotechnique* 31 (2), 181–213.

- Mackey, B.H., Roering, J.J., 2011. Sediment yield, spatial characteristics, and the long-term evolution of active earthflows determined from airborne LiDAR and historical aerial photographs, Eel River, California. *GSA Bull.* 123 (7/8), 1560–1576.
- Mackey, B.H., Roering, J.J., McKean, J.A., 2009. Long-term kinematics and sediment flux of an active earthflow, Eel River, California. *Geology* 37 (9):803–806. <http://dx.doi.org/10.1130/G30136A.1>.
- MesoWest, 2016. Website http://mesowest.utah.edu/cgi-bin/droman/station_total.cgi?stn=D0739&unit=0 accessed 15 March 2016.
- Messerich, J.A., Coe, J.A., 2003. Topographic map of the active part of the Slumgullion landslide on July 31, 2000, Hinsdale County, Colorado. U.S. Geological Survey Open-file Report 03-144 (Reston, VA).
- Milillo, P., Fielding, E.J., Schulz, W.H., Delbridge, B., Burgmann, R., 2014. COSMO-SkyMed spotlight interferometry over rural areas: the Slumgullion landslide in Colorado, USA. *IEEE J. Sel. Top. Appl. Earth Obs. Remote Sens.* 7 (7). <http://dx.doi.org/10.1109/JSTARS.2014.2345664>.
- Moore, P.L., Iverson, N.R., 2002. Slow episodic shear of granular materials regulated by dilatant strengthening. *Geology* 30 (9), 843–846.
- Oppikofer, T., Jaboyedoff, M., Blikra, L., Derron, M.-H., Metzger, R., 2009. Characterization and monitoring of the Aknes rockslide using terrestrial laser scanning. *Nat. Hazards Earth Syst. Sci.* 9, 1003–1019.
- Parise, M., 2003. Observation of surface features on an active landslide, and implications for understanding its history of movement. *Nat. Hazards Earth Syst. Sci.* 3, 569–580.
- Parise, M., Guzzi, R., 1992. Volume and shape of the active and inactive parts of the Slumgullion landslide, Hinsdale County, Colorado. U.S. Geological Survey Open-file Report 92-216 (Reston, VA).
- Parise, M., Moscarillo, A., Fleming, R.W., 1997. Evidence from flank ridges for long-term diminishing movement of the Slumgullion landslide, Hinsdale County, Colorado. U.S. Geological Survey Open-file Report 97-517 (Reston, VA).
- Parise, M., Coe, J.A., Savage, W.Z., Varnes, D.J., 2003. In: Picarelli, L. (Ed.), *The Slumgullion landslide (southwestern Colorado, USA): investigation and monitoring*. Proc. International Workshop "Occurrence and mechanisms of flow-like landslides in natural slopes and earthfills", May 14–16, 2003, Sorrento, pp. 253–263.
- Peng, Z., Gombert, J., 2010. An integrated perspective of the continuum between earthquakes and slow-slip phenomena. *Nat. Geosci.* 3:599–607. <http://dx.doi.org/10.1038/ngeo940>.
- Petley, D., 2012. Global patterns of loss of life from landslides. *Geology* 40 (10), 927–930.
- Pieraccini, M., Casagli, N., Luzi, G., Tarchi, D., Mecatti, D., Noferini, L., Atzeni, C., 2003. Landslide monitoring by ground-based radar interferometry: a field test in Valdarno (Italy). *Int. J. Remote Sens.* 24 (6), 1385–1391.
- Powers, P.S., Varnes, D.J., Savage, W.Z., 1992. Digital elevation models for Slumgullion landslide, Hinsdale County, Colorado based on 1985 and 1990 aerial photography. U.S. Geological Survey Open-file Report 92-535 (Denver, CO).
- Prokop, A., Panholzer, H., 2009. Assessing the capability of terrestrial laser scanning for monitoring slow moving landslides. *Nat. Hazards Earth Syst. Sci.* 9, 1921–1928.
- Reid, M.E., 1994. A pore-pressure diffusion model for estimating landslide-inducing rainfall. *J. Geol.* 102, 709–717.
- Reynolds, O., 1885. On the dilatancy of media composed of rigid particles in contact, with experimental illustrations. *Philos. Mag.* 5 (20), 469–481.
- Roering, J.J., Stimely, L.L., Mackey, B.H., Schmidt, D.A., 2009. Using DInSAR, airborne LiDAR, and archival air photos to quantify landsliding and sediment transport. *Geophys. Res. Lett.* 36, L19402. <http://dx.doi.org/10.1029/2009GL040374>.
- Rott, H., Scheuchl, B., Siegel, A., 1999. Monitoring very slow slope movements by means of SAR interferometry: a case study from a mass waste above a reservoir in the Ötztal Alps, Austria. *Geophys. Res. Lett.* 26 (11), 1629–1632.
- Savage, W.Z., Fleming, R.W., 1996. Slumgullion landslide fault creep studies. In: Varnes, D.J., Savage, W.Z. (Eds.), *The Slumgullion Earth Flow: A Large-scale Natural Laboratory*. U.S. Geological Survey Bulletin 2130. Reston, VA, pp. 73–76.
- Schlögel, R., Malet, J.-P., Doubre, C., Lebourg, T., 2015. Structural control on the kinematics of the deep-seated La Clapière landslide revealed by L-band InSAR observations. *Landslides* <http://dx.doi.org/10.1007/s10346-015-0623-0>.
- Schmidt, D.A., Bürgmann, R., 2003. Time-dependent land uplift and subsidence in the Santa Clara valley, California, from a large interferometric synthetic aperture radar data set. *J. Geophys. Res. B: Solid Earth* 108 (9) (ETG 4-1–4-13).
- Schmidt, K.M., Montgomery, D.R., 1995. Limits to relief. *Science* 270, 617–620.
- Schulz, W.H., Wang, G., 2014. Residual shear strength variability as a primary control on movement of landslides reactivated by earthquake-induced ground motion: implications for coastal Oregon, USA. *J. Geophys. Res. Earth Surf.* <http://dx.doi.org/10.1002/2014JF003088>.
- Schulz, W.H., McKenna, J.P., Biavati, Giulia, Kibler, J.D., 2007. Characteristics of Slumgullion landslide inferred from subsurface exploration, in-situ and laboratory testing, and monitoring. In: Schaefer, V.R., Schuster, R.L., Turner, A.K. (Eds.), 1st North American Landslide Conference, Vail, Colo., June 3–8, 2007. Proceedings: AEG Special Publication No. 23, pp. 1084–1097.
- Schulz, W.H., McKenna, J.P., Biavati, Giulia, Kibler, J.D., 2009a. Relations between hydrology and velocity of a continuously moving landslide – evidence of pore-pressure feedback regulating landslide motion? *Landslides* 6, 181–190.
- Schulz, W.H., Kean, J.W., Wang, G., 2009b. Landslide movement in southwest Colorado triggered by atmospheric tides. *Nat. Geosci.* 2 (12), 863–866.
- Schulz, W.H., Coe, J.A., Shurtleff, B.L., Panosky, J., Farina, P., Ricci, P.P., Barsacchi, G., 2012. Kinematics of the Slumgullion landslide revealed by ground-based InSAR surveys. In: Eberhardt, E., Froese, C., Turner, A.K., Leroueil, S. (Eds.), *Landslides and Engineered Slopes, Protecting Society Through Improved Understanding*. 2. Taylor & Francis Group, London, pp. 1273–1279.
- Schulz, W.H., Coe, J.A., Ricci, P.P., Smoczyk, G.M., Shurtleff, B.L., Panosky, J., Jones, E.S., 2016. Data Related to a Ground-based InSAR Survey of the Slumgullion Landslide, Hinsdale County, Colorado, 26 June 2010–1 July 2010. <http://dx.doi.org/10.5066/F7TX3CFW>.
- Skempton, A.W., 1985. Residual strength of clays in landslides, folded strata, and the laboratory. *Geotechnique* 35 (1), 3–18.
- Smith, W.K., 1993. Photogrammetric determination of movement on the Slumgullion slide, Hinsdale County, Colorado, 1985–1990. U.S. Geological Survey Open-File Report 93-597 (Reston, VA).
- SNOTEL Beartown, 2016. Website <http://wcc.sc.egov.usda.gov/nwcc/site?sitenum=327> accessed 15 March 2016.
- SNOTEL Slumgullion, 2016. Website <http://wcc.sc.egov.usda.gov/nwcc/site?sitenum=762> accessed 15 March 2016.
- Tarchi, D., Casagli, N., Moretti, S., Leva, D., Sieber, A., 2003. Monitoring landslide displacements by using ground-based synthetic aperture radar interferometry: application to the Ruinon landslide in the Italian Alps. *J. Geophys. Res.* 108 (B8). <http://dx.doi.org/10.1029/2002JB002204>.
- Terzaghi, K., 1931. Static rigidity of plastic clays. *J. Rheol.* 2, 253–262.
- Terzaghi, K., Peck, R.B., Mesri, G., 1996. *Soil Mechanics in Engineering Practice*. John Wiley & Sons, Inc., New York, NY.
- Tika, T.E., Vaughan, P.R., Lemos, L.J.L.J., 1996. Fast shearing of pre-existing shear zones in soil. *Geotechnique* 46 (2), 197–233.
- U.S. Geological Survey, 2005. Landslide hazards – a national threat. U.S. Geological Survey Fact Sheet 2005-3156 (Reston, VA).
- Varnes, D.J., Savage, W.Z., 1996. The Slumgullion earth flow: a large-scale natural laboratory. U.S. Geological Survey Bulletin 2130 (Reston, VA).
- Vulliet, L., Hutter, K., 1988. Continuum model for natural slopes in slow movement. *Geotechnique* 38 (2), 199–217.
- Walter, M., Gombert, J., Schulz, W., Bodin, P., Joswig, M., 2013. Slidequake generation versus viscous creep at softrock-landslides: synopsis of three different scenarios at Slumgullion landslide, Heumoes slope, and Super-Sauze mudslide. *J. Environ. Eng. Geophys.* 18 (4), 269–280.
- Wang, G., Suemine, A., Schulz, W.H., 2010. Shear-rate-dependent strength control on the dynamics of rainfall-triggered landslides, Tokushima Prefecture, Japan. *Earth Surf. Process. Landf.* 35, 407–416.
- Xing, C., Yu, Z.Q., Zhou, X., Wang, P., 2014. Research on the testing methods for IBIS-S system. IOP Conference Series: Earth and Environmental Science. 17:p. 012263. <http://dx.doi.org/10.1088/1755-1315/17/1/012263>.